

1 **Influence of the Madden Julian Oscillation on Precipitation and Surface Air**
2 **Temperature in South America**
3
4

5
6 Mariano S. Alvarez¹, C. S. Vera¹, G. N. Kiladis², B. Liebmann³
7

8 ¹Centro de Investigaciones del Mar y la Atmósfera, CONICET-UBA, DCAO/FCEN, UMI IFAECI/CNRS.
9 Buenos Aires, Argentina
10

11 ²NOAA/Earth System Research Laboratory
12

13 ³NOAA / Earth System Research Laboratory, and Cooperative Institute for Research in Environmental
14 Sciences, University of Colorado, Boulder, Colorado
15

Corresponding author address: Mariano S. Alvarez, CIMA, Ciudad Universitaria, Pabellón II-2do. Piso
(C1428EGA), Buenos Aires, Argentina.
E-mail: alvarez@cima.fcen.uba.ar

16 **Abstract**

17
18 The regional influence of the Madden-Julian Oscillation (MJO) on South America is described.
19 Maps of probability of weekly-averaged rainfall exceeding the upper tercile were computed for all seasons
20 and related statistically with the phase of the MJO as characterized by the Wheeler-Hendon Real-Time
21 Multivariate MJO (RMM) index and with the OLR MJO Index (OMI). The accompanying surface air
22 temperature and circulation anomalies were also calculated.

23 The influence of the MJO on regional scales along with their marked seasonal variations was
24 documented. During December-February when the South American monsoon system is active, chances of
25 enhanced rainfall are observed in southeastern South America (SESA) region mainly during RMM phases 3
26 and 4, accompanied by cold anomalies in the extratropics, while enhanced rainfall in the South Atlantic
27 Convergence Zone (SACZ) region is observed in phases 8 and 1. The SESA (SACZ) signal is characterized
28 by upper-level convergence (divergence) over tropical South America and a cyclonic (anticyclonic) anomaly
29 near the southern tip of the continent. Impacts during March-May are similar, but attenuated in the
30 extratropics. Conversely, in June-November, reduced rainfall and cold anomalies are observed near the coast
31 of the SACZ region during phases 4 and 5, favored by upper-level convergence over tropical South America
32 and an anticyclonic anomaly over southern South America. In September-November, enhanced rainfall and
33 upper-level divergence are observed in the SACZ region during phases 7 and 8. These signals are generated
34 primarily through the propagation of Rossby wave energy generated in the region of anomalous heating
35 associated with the MJO.

36
37 **Keywords:** Madden-Julian Oscillation, South America, precipitation, surface air temperature, impacts
38
39
40
41

42 1. Introduction

43

44 During the last decade it has been increasingly recognized that climate information, if it could be provided

45 weeks in advance, would be extremely important for decision making within many socio-economic sectors.

46 Such information relies on the monitoring and prediction of the intraseasonal (IS) variability and in particular

47 of the Madden-Julian Oscillation (MJO). MJO impacts have been assessed globally (e.g., Donald et al. 2006)

48 and regionally for different parts of the world, such as for the United States (Zhou et al. 2012; Jones et al.

49 2011), Chile (Barret et al. 2012), the Caribbean (Martin and Schumacher 2011), Australia (Wheeler et al.

50 2009), Southeast China (Zhang et al. 2009), India (Pai et al. 2009), Mexico and Central America (Barlow et

51 al. 2006) and East Africa (Pohl and Camberlin 2006), and in many other regions (see Lau and Waliser 2012).

52 Precipitation in South America exhibits considerable variability on IS timescales in all seasons (e.g.,

53 Liebmann et al. 1999 for austral summer and Alvarez et al. 2013 for austral winter). During summer, Nogues-

54 Paegle and Mo (1997) detected a dipole in the IS variability of convection, a pattern that shows centers of

55 action of opposite signs between the South American convergence zone (SACZ) and southeastern South

56 America (SESA). The MJO influence in South America has been identified in both austral summer

57 precipitation (e.g., Liebmann et al. 2004, Jones et al. 2004, De Souza and Ambrizzi 2006) and in the

58 occurrence of extreme wet and dry events (e.g., Muza et al. 2009). A large modulation of precipitation by the

59 MJO in the area of the SACZ has been found (e.g., Paegle et al. 2000; Carvalho et al. 2004). Furthermore,

60 large IS variability has also been recorded in surface air temperature anomalies in southern South America

61 (e.g., Cerne and Vera 2011), which seems to be at least partially influenced by MJO activity (Naumann and

62 Vargas 2010).

63 Nevertheless, detailed knowledge of the MJO influence on South America climate is still quite

64 incomplete. A more detailed description of the influence of the MJO on rainfall, temperature and circulation

65 as well as its seasonal variations would provide a fundamental basis for MJO monitoring in the region. This

66 work is inspired by the study of Wheeler et al. (2009), who quantified the MJO influence on precipitation in

67 Australia. This has allowed operational monitoring of that influence by the Australian Bureau of Meteorology

68 (<http://www.bom.gov.au/climate/mjo/>).

69 The aim of this work is to provide a quantitative analysis of the variability of both precipitation and

70 temperature explained by the MJO in South America, and a discussion of the large-scale circulation

71 anomalies that account for that influence. The study covers the entire seasonal cycle, as both regional climate
72 and MJO activity have a strong seasonality. The paper is organized as follows: Section 2 describes the data
73 and methodology used; Section 3 describes the seasonal evolution of regional climate anomalies in South
74 America associated with MJO activity as well as the associated large-scale circulation anomalies; and
75 conclusions are presented in Section 4.

76

77 2. Data and Methodology

78

79 **Data**

80

81 Daily values of 250-hPa geopotential heights, 0.21-sigma level velocity potential, and surface air
82 temperature were taken from the National Center for Environmental Prediction – National Center for
83 Atmospheric Research (NCEP-NCAR) reanalysis dataset (Kalnay et al. 1996), from December 1979 to
84 November 2012. These datasets are on a 2.5°x 2.5° grid. Daily precipitation on a 1°x1° grid is from the dataset
85 developed by Liebmann and Allured (2005), within the period December 1979 to November 2011.

86 Wheeler and Hendon (2004) constructed the Real-time Multivariate (RMM) index to monitor MJO
87 evolution. They used the two leading empirical orthogonal functions (EOFs) of the combined fields of
88 normalized 850-hPa zonal wind, 200-hPa zonal wind and outgoing longwave radiation (OLR) data averaged
89 from 15S-15N. The RMM index is defined from the two principal component time series, with RMM1
90 associated with EOF1 and RMM2 with EOF2. The index is used to describe the temporal evolution of the
91 amplitude and phase of the MJO and is divided into 8 phases, according to the region in which convection is
92 enhanced. The same EOF pair is used for the entire year, and despite strong seasonality in the latitude of
93 convection, during all seasons in phases 8 and 1 convection is maximum in the western hemisphere and
94 Africa, phases 2 and 3 correspond to a maximum over the Indian Ocean, phases 4 and 5 peak over the
95 Maritime Continent, and phases 6 and 7 over the western Pacific (Wheeler and Hendon 2004). It has been
96 shown that statistical prediction of the RMM index has useful skill out to two weeks by using RMM1 and
97 RMM2 as predictors at an initial time (Maharaj and Wheeler 2005).

98 The analysis presented here was repeated with an OLR only based MJO index (OMI) derived by Kiladis et
99 al. (2014). This index is based on the first two EOFs of “MJO-filtered” OLR, calculated daily using a sliding
100 121 day window to take into account the seasonal migration of the MJO OLR activity. Since RMM is

101 dominated by the circulation component of the MJO (Straub 2013), there can be substantial differences
 102 between the amplitude and phase of the OMI and RMM for individual MJO events, although differences are
 103 less pronounced for statistical results using either index (Kiladis et al. 2014). Results for this study were quite
 104 similar using either index, so we focus on the results for RMM for consistency with Wheeler et al. (2009). A
 105 brief discussion and some examples of the RMM-OMI comparison can be found in the Appendix.

106

107 **Methodology**

108

109 All calculations were done separately for the 3-month seasons December-February (DJF), March-May
 110 (MAM), June-August (JJA) and September-November (SON). Daily anomalies of temperature, geopotential
 111 height and velocity potential were calculated at every grid point by subtracting the long-term average for that
 112 day so as to remove the seasonal cycle.

113 Following Zhou et al. (2011), composites of temperature, geopotential height and velocity potential
 114 anomalies were generated for each MJO phase through regression modeling. The advantage of the regression-
 115 based approach is that it fits the regression model to observations from all phases (without reducing the
 116 dataset length). The linear model presented by Zhou et al. (2011) was used in this study, to quantify the linear
 117 response (E) of a given atmospheric variable to the MJO at a certain location. At every grid point a linear
 118 regression is then computed using RMM1 and RMM2 (hereafter x_1 and x_2) as predictors, obtaining two
 119 regression constants, β_1 and β_2 ; that is

$$E = \beta_1 x_1 + \beta_2 x_2$$

120 which can be written as,

$$E = \gamma_1 A \cos(\theta - \gamma_2)$$

121 where $\gamma_1 = \sqrt{\beta_1^2 + \beta_2^2}$ scales the instantaneous amplitude of the MJO ($A = \sqrt{x_1^2 + x_2^2}$) and $\gamma_2 =$
 122 $\tan^{-1}(\beta_2/\beta_1)$ shifts its phase $\theta = \tan^{-1}(x_2/x_1)$.

123 It is possible to estimate for every grid point and for a given phase the expected response in order to
 124 generate composites using a fixed amplitude, which was set in this study to its mean value, while varying
 125 x_1 and x_2 to define the phase according to the phase-space defined by x_1 and x_2 . For example, θ in MJO
 126 phase 5 was set to $\pi/8$, in MJO phase 6 to $3\pi/8$ and so on, adding $\pi/4$ for the next phase in a counter-

127 clockwise direction. Since all phases are used to fit the regression, a sinusoidally varying model is produced,
128 so, for example, MJO phases 5 and 1 are the exact opposites, as their phases are shifted by π .

129 Two maps can be constructed to describe the composites: a map of γ_1 , that shows the amplitude of the
130 response E to a complete cycle of the MJO, and a map of γ_2 , that shows the phase at which E is maximum.
131 These maps are known as coamplitude and cophase maps. If the instantaneous amplitude of the MJO is
132 smaller than 1, then it is considered a neutral MJO day. Statistical significance of the composites was tested as
133 in Zhou et al. (2011), who used Monte Carlo techniques to create an approximated sampling distribution of
134 the coefficient of determination, assuming that the dependent variable is not related to the dependent variables
135 (x_1 and x_2).

136 Composites for rainfall were computed following Wheeler et al. (2009), although they explored additional
137 rainfall metrics than the present study. Wheeler et al. (2009) computed daily anomalies and the probability of
138 7-day running mean rainfall exceeding different thresholds: the upper tercile, the highest decile and 1 mm
139 day⁻¹. Wheeler et al. (2009) concluded that the probability of exceeding the weekly tercile was the most
140 appropriate metric, as they are less influenced by outliers than daily anomalies, and occur more frequently
141 than highest decile events, therefore achieving greater statistical confidence in the results. Furthermore, as the
142 upper-tercile threshold fluctuates with location and season, it is more appropriate than a constant metric.
143 Hence, the upper tercile was the metric chosen for this study.

144 The tercile exceedences were computed from 7-day running mean precipitation. For each phase the
145 number of days in which weekly rainfall was above the upper tercile (67th percentile) was counted and divided
146 by the total number of days in each phase to obtain the probability of exceeding the threshold. Therefore, the
147 probability composites for each phase show the chance that precipitation has exceeded the upper tercile at a
148 given location during that phase. The composites are scaled by the local mean probability of exceeding the
149 threshold, which is nominally 33%. Statistical significance was tested following the nonparametric re-
150 sampling approach proposed by Wheeler et al. (2009), which consists of generating 400 synthetic realizations
151 of the probability composites, obtained by successively shifting the time sequence of the observed MJO
152 phases relative to the rainfall time series, to create the null distribution with which to compare the composite.

153

154 3. Results

155

156 **a. Large-scale dynamics**

157

158 The influence of the MJO on circulation anomalies in the vicinity of South America can be exerted mainly
159 by two different ways: i) changes in the tropical circulation associated to the eastward passage of MJO
160 diabatic heating anomalies along the equator; and ii) changes in the extratropical circulation anomalies
161 through Rossby wave trains extending between tropical western Pacific-Indian Ocean sector and South
162 America (Berbery and Noguez-Paegle 1993; Mo and Higgins 1998; Kiladis and Mo 1998; Kidson 1999;
163 Revell et al. 2001). During austral summer, changes in the divergent tropical circulation can enhance or
164 inhibit convection associated with the South American Monsoon System (SAMS), mainly within the SACZ,
165 which in turn impacts the vertical motion in the subtropics. At the same time, regional circulation anomalies
166 mainly over southern South America can be influenced by the large-scale extratropical circulation anomalies
167 in turn induced by the convection enhanced or suppressed by the MJO over tropical western Pacific-Indian
168 tropical oceans. While these two mechanisms have been highlighted in previous works focused on summer
169 (e.g., Cavalho et al. 2004, Liebmann et al. 2004), neither their combined influence over South America nor
170 their seasonality have been explored in detail.

171 The following sub-sections focus on the circulation anomalies associated to MJO that can help to explain
172 the MJO signals of both rainfall and temperature anomalies identified in South America. Composites of large-
173 scale anomalies of geopotential height at 250 hPa and velocity potential at 0.21 sigma-level are analyzed as
174 the key features associated with the extratropical and tropical circulation changes, respectively. They are
175 presented in Figures 1-4 for each season and for MJO phases 1 to 4, which, with the opposite sign, are to be
176 interpreted as MJO phases 5 to 8. Note that the eastward MJO propagation, depicted by the upper-level
177 velocity potential anomalies along the tropics (Figs. 1-4), represents the mean evolution of the oscillation.
178 Individual MJO events may not have such coherent behavior.

179

180 **i. December-February**

181 Anomalous upper-level tropical convergence (represented by positive velocity potential anomalies)
182 progresses eastwards from western tropical Pacific during phase 1 and arrives in tropical South America by
183 phases 4 and 5 (Fig. 1), inhibiting upward motion in that region. At the same time, between phases 2 and 5, a

184 Rossby wave train develops between Australia and the Bellinghausen - Amudsen Seas and is refracted
185 equatorward, resulting in an extratropical cyclonic anomaly over subtropical South America. Its development
186 promotes anomalous upward motion over SESA and subsidence in the SACZ region.

187 On the other hand, from phases 6 to 1, anomalous upper-level tropical divergence (indicated by negative
188 velocity potential anomalies) progresses from the western tropical Pacific and reaches tropical South America
189 by phase 8, (Fig. 1) where it favors anomalous upward motion through phase 1 and consequently inhibits
190 upward motion in the corresponding subtropics due to compensatory subsidence. In addition, through phases
191 6 to 1, a Rossby wave train extends between Indian-western Pacific tropical oceans and South America,
192 which contributes to the development of an anticyclonic anomaly in the southern tip of the continent that also
193 favors subsidence in the subtropics and extratropics of South America.

194

195 **ii. March-May**

196 The tropical divergent circulation anomalies in MAM (Fig. 2) are similar to those observed in summer
197 (Fig. 1), inhibiting upward motion over tropical South America mainly between phases 4 and 5 and favoring it
198 mainly between phases 8 and 1 (Fig. 2). During this season, however, the extratropical Rossby wave train,
199 which emerges from the anomalous equatorial convection in the equatorial Indian Ocean (Fig. 2, phases 3-5
200 and 7-2), propagates poleward farther to the west than in summer. This results in less influence of the
201 rotational circulation anomalies over the continent. As a consequence, the associated cyclonic circulation
202 anomaly is over the southeastern Pacific (Fig. 2, phases 2-4), whereas during summer it was centered over the
203 tip of the continent (Fig. 1, phases 1-4). This feature therefore contributes less to inducing anomalous upward
204 motion in SESA. The opposite happens with the Rossby wave train observed between phases 6 and 1, which
205 is related to an anticyclonic circulation anomaly located over the southeastern Pacific, farther to the west than
206 in summer.

207

208 **iii. June-August**

209 During winter, significant changes are observed in the behavior of the extratropical Rossby wave train as
210 compared to that observed in summer and fall. The Rossby wavetrain emerging from the Indian Ocean
211 observed in winter is associated with a more zonally oriented circulation anomaly pattern with a lower

212 planetary wave number that extends more towards the Antarctic coast, closer to the Antarctic Peninsula (Fig.
213 3). Furthermore, a zonally oriented Rossby wave train is discernible mainly between phases 3 and 4 (and with
214 opposite sign between phases 7 and 8) in the subtropical latitudes of the South Pacific, likely favored by the
215 presence of the winter mean subtropical jet. Such combination of wave trains evolving at both subtropical and
216 subpolar latitudes of the South Pacific has also been identified in previous works of austral winter IS
217 variability (e.g., Alvarez et al. 2013). Between phases 2 and 4 (6 and 8), an anticyclonic (cyclonic) anomaly
218 in subtropical South America and cyclonic (anticyclonic) one further south are evident.

219 Regarding the divergent circulation, upper-level divergence is observed over the continent during MJO
220 phases 8 and 1, favoring ascent in the region, while the opposite is found when upper-level convergence
221 anomalies associated with MJO cross the continent mainly between phases 4 and 5 (Fig. 3). In particular, the
222 features observed between phases 2 and 3 agree broadly with that identified by Alvarez et al. (2013) in
223 association with the wet phase of the activity of the leading pattern of rainfall variability on IS timescales,
224 which is characterized by a spatial monopole extended over tropical South America.

225

226 **iv. September-November**

227 During this trimester the rainy season onset occurs on average in tropical South America and both SAMS
228 and SACZ related convection develops (e.g. Vera et al. 2006). Moreover, tropical divergent circulation
229 anomalies associated with MJO activity (Fig. 4) evolve quite similarly to those observed in DJF (Fig. 1).
230 During phases 7 to 1 (4 and 5) upper-level divergence (convergence) is evident over tropical South America,
231 promoting chances of upward (downward) motion over the SAMS-SACZ region (Fig. 4). On the other hand,
232 the mean extratropical circulation in the South Pacific during this season shares some similarities to that
233 observed in winter (Fig. 3). In particular, the Rossby wave train associated to MJO activity is very well
234 defined and coherent along the high-latitude South Pacific, except that it exhibits an equatorward bend at
235 around 110W compared to the pattern in winter (Fig. 3). Consequently, this refraction and the equatorward
236 propagation are mainly along the southwestern Atlantic Ocean, influencing the circulation anomalies in the
237 continent to a lower degree.

238

239 **v. Coamplitude and cophase**

240 The characteristics of the large-scale circulation anomalies described above are summarized in Figure 5,
241 which shows for each season the maps of coamplitude (defined in section 2) for 250-hPa geopotential height
242 anomalies associated with MJO activity. In DJF, the signal extends from Australia southeastward to
243 Bellinghausen - Amundsen seas and refracts equatorward over South America, with the largest amplitude to
244 the north of Ross Sea. In MAM, the signal is much weaker in general and the pattern seems to be refracted at
245 higher latitudes and farther west than in DJF, so the influence over South America is less evident. In JJA, the
246 signal has increased, it is very coherent, and it seems to be associated with a lower planetary wave number
247 than in the previous season. During this season, the signal is refracted near the Antarctica coast and at a
248 longitude closer to the Antarctica Peninsula. A zonally oriented Rossby wave train of moderate amplitude
249 along the subtropical latitudes of the South Pacific is also evident. In SON the Rossby wave train arching
250 between Australia and the South Atlantic has the largest amplitude among all seasons and it is also very
251 coherent. It refracts equatorward at the same longitude than in winter but at lower latitude, while the signal
252 continues to be very large and coherent well into the South Atlantic Ocean. On the other hand, no signal
253 associated with subtropical wave trains is discernible in this season.

254 Figure 6 shows the cophase (defined in section 2) of the 250-hPa negative-geopotential height anomalies
255 associated with MJO activity. Each color defines the phase at which the cyclonic anomaly of geopotential
256 height is most intense at a certain location. In the subtropics from the Indian Ocean to South America, the
257 phase increases smoothly at all seasons, indicating the eastward-propagating MJO signal in the circulation.
258 Within the extratropics, there is evidence of the signal propagating along an arch between mainly Indian
259 Ocean-Australia sector and South America-South Atlantic sector but with large seasonal variation. In DJF,
260 there is a dominant cyclonic signal at the SACZ oceanic portion location on phases 7-8-1, while further south
261 it is during phases 3-4. In MAM, the most evident signal over South America is within the tropical regions
262 during phases 7-8, while there is no signal at the southern tip of the continent. On the other hand, in JJA the
263 cyclonic signal goes from central South America during phase 7 to both equatorward and poleward in phases
264 8-1 and even in phase 2 in Patagonia. In SON, while both the subtropical and northern portion of South
265 America exhibit significant signal between phases 1 and 2, in the SACZ region this is present in phases 7 and
266 8.

267 Overall, the results of this subsection substantiate the fact that in the mean, MJO heating initiates Rossby
268 wave energy propagation into the South Pacific sector, some of which refracts equatorward over the South
269 American sector, with the amount varying by season. At the same time, the tropical portion of the MJO
270 dynamical signal also induces circulation anomalies over tropical South America that would either favor or
271 disfavor convective activity. We now examine the impacts of these circulations on the surface variability over
272 South America.

273

274 **b. Daily temperature composites**

275

276 Daily temperature anomalies were composited according to a mean-amplitude MJO, for each MJO phase,
277 and by season. During DJF (Fig. 7), warm anomalies are present over the extratropical part of the continent
278 from phase 6 to 1, when anomalous downward (upward) motion is favored over the SESA (SACZ) region
279 (Fig. 1). This is in agreement with the mechanism described by previous works (e.g., Cerne et al 2007):
280 compensatory subsidence over subtropical South America, clear skies and diabatic warming is promoted
281 during enhanced convection over the SACZ region. On the other hand, cold anomalies are more intense over
282 extratropical South America from phases 2 to 5. We note that the vertical structure of the extratropical
283 anomalies isolated in this study are nearly equivalent barotropic, with only a slight southwestward tilt with
284 height (not shown), as was found in previous studies (e.g. Liebmann et al. 2004). Thus the cold anomalies
285 over extratropical South America in these phases can be related to cold advection and the anomalous upward
286 motion promoted in turn by the cyclonic anomaly observed over this region (Fig. 1). Temperature anomalies
287 are large over northern Patagonia, central-western Argentina and central Chile. Northeastern Brazil also
288 shows cold (warm) anomalies in phases 1 to 3 (5 to 7).

289 In MAM (Fig. 8), cold (warm) anomalies are stronger mainly over northern Chile, western Bolivia,
290 eastern Paraguay and southern Brazil from phases 8 to 2 (4 to 6), when anomalous upward (downward)
291 motion is favored due to the cyclonic (anticyclonic) anomaly observed in the region. Meanwhile, warm
292 (cold) anomalies are observed within northwest South America. Throughout JJA (Fig. 9) significant cold
293 (warm) anomalies are observed in phase 8 (4) over northern Chile and extending to the south and west in
294 phases 1 to 3 (5 to 6), which can be associated with the cyclonic (anticyclonic) anomaly located in southern
295 South America (Fig. 3).

296 In SON (Fig. 10), warm anomalies extend from central Chile and central-western Argentina towards
297 northwestern Argentina and Paraguay from phases 6 to 8, explained both by warm advection from the north
298 and also partially by compensatory subsidence conditions promoted by the upper-level divergence located
299 over tropical South America (Fig. 4). The latter is similar to the mechanism described during summer. The
300 southwestern Atlantic Ocean also shows significant warm anomalies during these phases, and in phase 8 cold
301 anomalies start to develop over the continental SACZ region, which are evident until phase 2. On the other
302 hand, the subtropical regions of the continent exhibit cold anomalies from phases 2 to 4, as does the
303 southwestern Atlantic Ocean, which is the result of cold advection between the large anticyclone over the
304 Amundsen Sea in combination with the strong South Atlantic cyclone in Fig. 4. From phases 4 to 6 warm
305 anomalies are observed over the SACZ region, a signal at least in part due to the tropical subsidence induced
306 by upper level convergence.

307

308 **c. Weekly rainfall probability**

309

310 In this section we discuss changes in South American precipitation variations associated with the MJO. As
311 discussed above, these are quantified in terms of the probability of precipitation exceeding the upper tercile.
312 The probabilities are scaled such that a greater (less) than 1.0 ratio of probabilities would mean an increased
313 (reduced) chance of above-threshold precipitation during a certain phase of the MJO. As an example, a ratio
314 of 1.5 (0.5) would mean that the chance of exceeding the threshold was increased (reduced) by 50%. As the
315 nominal probability of exceeding the upper tercile is 33%, a ratio of 1.5 (0.5) during a certain phase means
316 that there is a 49.5% (16.5%) of probability of exceeding the threshold during that phase. Maps of the mean
317 seasonal rainfall, the value of the event threshold and the composite for the neutral MJO cases are also shown
318 for reference. Changes in precipitation are related with those identified in the circulation anomalies at large
319 and regional scales (Figs. 1-4). Such analysis provides some indications of the mechanisms explaining the
320 MJO impact on the precipitation. A more detailed study of the dynamic and thermodynamic processes
321 involved is beyond the scope of the present work.

322 During DJF (Fig. 11), there is an increased probability of above-threshold precipitation in eastern Brazil
323 during phase 1, which disappears in phase 2 except along the northern coast. During phases 3 and 4 there are
324 ratios in excess of 1.6 over SESA, as well as lower than 1.0 ratios in the continental portion of the SACZ, a

325 pattern of summer variability that resembles the dipole first described by Nogues-Paegle and Mo (1997). This
326 can be related to anomalous upward motion over SESA promoted by the cyclonic anomaly observed over
327 extratropical South America (Fig. 1). Furthermore, during phase 4 there is an increased chance of exceeding
328 the threshold in central eastern Argentina. Centered on phase 5, but also distinguishable in phases 4 and 6,
329 there is a dramatic decrease in probabilities over most of eastern Brazil, including the climatological SACZ
330 region, with the ratios less than 0.4 in some regions. The reduced probabilities are associated with the
331 anomalous upper-level tropical convergence that produces subsidence, consistent with positive velocity
332 potential anomalies in Fig. 1. In MJO phase 8, central and eastern Brazil shows regions of ratios in excess of
333 1.2, in association with upper-level divergence over that region (Fig. 1).

334 During neutral MJO conditions (lower-right panel of Fig. 11), the probability of exceeding the threshold in
335 the position of the climatological SACZ (in SESA) is slightly above (below) 1.0 ratio, and there is no other
336 large region with a marked influence of MJO. Furthermore, the SACZ and SESA have been previously
337 identified as having large IS variability also on timescales closer to 20 days (e.g., Gonzalez and Vera 2013),
338 associated with alternating centers of enhanced and suppressed precipitation between those two regions (e.g.,
339 Paegle et al. 2000).

340 In MAM (Fig. 12), during phase 2 and to a lesser extent in phases 1 and 3, much of eastern Brazil exhibits
341 elevated probabilities, though the large scale circulation might be able to explain this only during phase 1,
342 given that upper-level divergence is observed over tropical South America as well as a cyclonic anomaly over
343 SESA (Fig. 2). An area of eastern Brazil with ratios below 1 appears in phase 4, and continues to expand
344 through phase 6, when low ratios are prevalent over most of eastern Brazil. At the same time ratios above 1
345 are observed in SESA, although the associated circulation anomaly pattern is not clear. This area switches to
346 negative by phase 8. During other phases and neutral conditions, only scattered areas of abnormal
347 probabilities are evident.

348 JJA is the dry season throughout tropical South America and there are fewer areas of coherent ratios than
349 in the other seasons. During phases 8 and 1, however, greater chances of enhanced rainfall are observed in
350 northern South America (Fig. 13) in association with the passage across the continent of the upper-level
351 divergence anomalies associated with MJO (Fig. 3). The opposite is found when the upper-level convergence
352 anomalies associated with MJO cross the continent mainly between phases 4 and 5. The far northwest of the

353 continent seems to be particularly responsive to these circulation changes, as there is an increased probability
354 of enhanced rainfall in phases 8, 1 and 2, a probability which turns to lower than nominal during phases 4 and
355 5. MJO phase 8 also shows excess ratios in southeastern Brazil (Fig. 13). The regional circulation
356 configuration may explain this, as during phase 8 a cyclonic anomaly is observed in eastern subtropical South
357 America, which would force upward motion over the region (Fig.3).

358 SON (Fig. 14) shares characteristics with both summer and winter. During phases 4 and 5 ratios are
359 smaller than 1.0 in eastern Brazil, but they are weaker than those observed in DJF. The prominent dipole of
360 the summer, present to a lesser extent in MAM, is distinctly missing in SON. On the other hand, during phase
361 7 enhanced ratios are observed in the region of Brazil centered at 15S. Similar to JJA, a cyclonic anomaly
362 centered at around 20S enhances upward motion, which would promote enhanced rainfall over this region
363 (Fig. 4). On the contrary, the opposite flow configuration between phases 3 and 5 would reduce the chances of
364 enhanced rainfall.

365 Further south, the cyclonic anomaly that evolves from west of the Antarctic Peninsula in phase 7, to
366 subtropical South America on phase 1 (Fig. 4) appears to develop favorable conditions for enhanced
367 precipitation over SESA during that phase. Accordingly, the anticyclonic anomaly located over southern
368 South America during phases 6 and 7 seems to reduce chances of enhanced rainfall over SESA (Fig. 14).
369 During neutral MJO conditions the pattern of ratios is mostly scattered.

370

371 4. Conclusions

372 The impact of the MJO on precipitation and surface air temperature over South America was analyzed,
373 providing a reference about the timing and intensity of MJO signal over this continent that can be used for
374 monitoring and prediction activities in the region. The precipitation changes associated with MJO activity
375 were quantified following Wheeler et al. (2009), in probabilistic terms of the probability of exceeding the
376 upper tercile of the weekly-averaged rainfall distribution. In addition, the anomalies of surface air temperature
377 in South America and large-scale upper-level circulation in the Southern Hemisphere were described using
378 the linear regression model proposed by Zhou et al. (2011). The signals were obtained with respect to the
379 Wheeler and Hendon (2004) RMM index, and were found to be robust for the most part when using the OLR-
380 only derived index of Kiladis et al. (2014) as shown in the Appendix.

381 MJO influence on regional climate in South America was detected in all seasons, but with large seasonal
382 variations. In DJF, when the SAMS is active, increased chances of precipitation exceeding the upper tercile
383 are observed in the SESA (SACZ) regions mainly between phases 3 and 4 (8 and 1). Such a pattern is favored
384 by upper-level convergence (divergence) over tropical South America and a cyclonic (anticyclonic) anomaly
385 around its southern tip, both being circulation responses to MJO activity. During MAM, the impacts are
386 somewhat similar to those observed in DJF except that the extratropical Rossby wave train influences
387 extratropical South America to a lower degree. On the other hand, in JJA and SON, during the dry season in
388 the tropics, reduced chances of rainfall exceeding the upper tercile are observed in SACZ mainly between
389 phases 4 and 5, favored by upper-level convergence over tropical South America and an anticyclonic anomaly
390 located further south, both being circulation responses to MJO activity.

391 Results suggest that the SAMS activity induces a large modulation on the MJO influence on climate
392 variability in South America. It is also evident that in all seasons circulation anomalies over South America
393 that in turn induce both precipitation and surface air temperature anomalies are a combination between the
394 divergent circulation response to MJO with largest amplitude at the tropics and the rotational circulation
395 response to MJO, with largest amplitude at the extratropics. However, the controlling mechanisms of the
396 circulation response, such as timing and signal location over both South America and the South Pacific
397 Ocean, require further investigation. Therefore, an improved understanding of the tropical-extratropical
398 processes associated with the MJO signal propagation over the South Pacific from the Indian Ocean-Australia
399 sector towards South America-South Atlantic sector will be the purpose of a future study.

400

401 Appendix

402

403 The phase of the OMI was made directly comparable to RMM Index following Kiladis et al. (2014), and
404 the calculations in this work were then repeated using that index. As the RMM Index is constructed using
405 OLR and circulation, it was expected for the RMM composites to show more signal overall, particularly in the
406 geopotential height anomalies composites. As an example, Figure 15 and 16 shows the large-scale anomalies
407 of geopotential height at 250 hPa and velocity potential at 0.21 sigma-level and for MJO phases 1 to 4, which,
408 with the opposite sign, are to be interpreted as MJO phases 5 to 8, for DJF and SON respectively.

409 The OMI-based (Fig. 15) and the RMM index-based (Fig. 1) composites for the DJF season are
410 remarkably similar. The extent of the statistically significant signals and the amplitude of the anomalies are
411 generally reduced, although the locations of the centers agree well. The OMI-based composites for MAM and
412 JJA (not shown) also resulted comparable to the RMM index-based, though some centers over the southern
413 Indian Ocean presented larger amplitude when using the OMI during MAM. During JJA, significance spans
414 slightly larger regions using RMM index, and is particularly strong to the southwest of South America on
415 phases 1 and 2 (and 5 and 6, Fig. 3), which was not the case when using OMI.

416 Table 2 of Kiladis et al. (2014) shows that the OMI leads the RMM Index by 4 days in SON, being the
417 greatest lag of the four seasons. It was therefore expected that we would find the greatest differences in the
418 composites during SON. Figure 16 shows that phases 2, 3 and 4 of the OMI-based composites may be
419 associated to phases 1, 2 and 3 of the RMM Index-based composites respectively (Fig. 4), consistent with the
420 lag between the indexes. The OMI-based composites (Fig. 16) did not show a significant signal to the
421 southwest of South America, and significance and amplitude of the centers were reduced compared to RMM
422 index-based composites (Fig. 4).

423 Figures 17 and 18 show the rainfall probability composites for DJF and SON respectively, analogous to
424 Figures 11 and 14 but using the OMI as opposed to the RMM index. Again, during DJF both composites
425 results are quite alike (Figs. 11 and 17), although the OMI-based probability composites seem to have
426 significant signal over more regions of South America, with a few exceptions, as eastern Brazil in MJO phase
427 8 and during neutral MJO cases, when OMI-based composites do not show a coherent signal (Fig. 17). During
428 MAM, the OMI-based composites (not shown) are overall similar to RMM index-based ones, however, the
429 most remarkable discrepancies are that the former showed a stronger signal with ratios lower than 1 over
430 SESA (eastern Argentina) on MJO phase 1 (3) and greater than 1 ratios over SESA and west of the South
431 Brazilian Bight on MJO phase 8. During JJA, OMI-based composites are seen to have an overall larger signal
432 (not shown), though these signals are, as in RMM-based composites, less coherent than in the other seasons.

433 As previously seen with the circulation composites, during SON, OMI-based rainfall probability
434 composites (Fig. 18) lead RMM index-based ones (Fig. 14) by one MJO-phase, that is, OMI-based composite
435 on MJO phase 1 resembles the RMM index-based composite during MJO phase 8, and so on. The most

436 remarkable differences when comparing both composites were observed over eastern Argentina and SESA,
437 though the general pattern resulted similar.

438 The OMI-based temperature composites (not shown) presented overall less regions with statistically
439 significant signal. The regional pattern observed in DJF was quite similar to the RMM index-based
440 composites (Fig. 7), the latter presenting higher values over northern Patagonia. During MAM, RMM index-
441 based composites showed significance over SESA and slightly higher anomalies over the continent compared
442 to the OMI-based composites, while during JJA the extratropical significant signal using OMI was
443 considerably reduced. Finally, during SON, the lag observed in the comparison with the other variables was
444 also present in temperature composites. In particular, the signal over northwestern Argentina and in the South
445 Atlantic Ocean was noticeably reduced when the OMI was used. The fact that OMI signals are comparable to
446 those using RMM is reassuring, although it is perhaps not surprising that in some cases there is less
447 significance to the OMI results, since a significant portion of the RMM signal is likely related to circulation
448 anomalies over the South America sector (Straub 2013; Kiladis et al. 2014).

449

450 **Acknowledgments**

451 This research was supported by UBACyT 20020100100434, ANPCyT PICT-2010-2110. M.A. is
452 supported by a Ph.D grant from CONICET, Argentina.

453

454 **References**

- 455 Alvarez MS, Vera CS, Kiladis GN, Liebmann B (2013) Intraseasonal variability in South America during
456 the cold season. *Clim Dyn.* doi:10.1007/s00382-013-1872-z
- 457 Barret BS, Carrasco JF, Testino AP (2012) Madden-Julian Oscillation (MJO) modulation of atmospheric
458 circulation and Chilean winter precipitation. *J Clim* 25(5): 1678-1688
- 459 Barlow M, Salstein D (2006) Summertime influence of the Madden-Julian Oscillation on daily rainfall
460 over Mexico and Central America. *Geophys Res Lett* 33:L21708. doi:10.1029/2006GL027738
- 461 Berbery EH, Nogues-Paegle J (1993) Intraseasonal interactions between the tropics and extratropics in
462 the Southern Hemisphere. *J Atmos Sci* 50(13):1950-1965
- 463 Carvalho LMV, Jones C, Liebmann B (2004) The South Atlantic convergence zone: intensity, form,
464 persistence, relationships with intraseasonal to interannual activity and extreme rainfall. *J Clim* 17:88–
465 108

466 Cerne B, Vera CS, Liebmann B (2007) The nature of a heat wave in eastern Argentina occurring during
467 SALLJEX. *Mon Weather Rev* 135:1165-1174

468 Cerne B, Vera C (2011) Influence of the intraseasonal variability on heat waves in subtropical South
469 America. *Clim Dyn* 36:2265–2277

470 De Souza EB, Ambrizzi T (2006) Modulation of the intraseasonal rainfall over tropical Brazil by the
471 Madden-Julian oscillation. *Int J Clim* 26(13):1759-1776

472 Donald A, Meinke H, Power B, deMaia AHN, Wheeler MC, White N, Stone RC, Ribbe J (2006) Near-
473 global impact of the Madden-Julian Oscillation on rainfall. *Geophys Res Lett* 33:L09704.
474 doi:10.1029/2005GL025155

475 Gonzalez PLM, Vera CS (2013) Summer precipitation variability over South America on long and short
476 intraseasonal timescales. *Clim Dyn*. doi:10.1007/s00382-013-2023-2

477 Jones C, Gottschalck J, Carvalho LMV, Higgins WR (2011) Influence of the Madden–Julian oscillation
478 on forecasts of extreme precipitation in the contiguous United States. *Mon Weather Rev* 139:332–350

479 Jones C, Waliser DE, Lau KM, Stern W (2004) Global occurrences of extreme precipitation events and
480 the Madden–Julian oscillation: observations and predictability. *J Clim* 17:4575–4589

481 Kalnay E et al (1996) The NCEP/NCAR 40-year reanalysis project. *Bull of the Am Meteorol*
482 *Soc* 77(3):437-471

483 Kidson JW (1999) Principal modes of Southern Hemisphere low-frequency variability obtained from
484 NCEP-NCAR reanalyses. *J of Clim* 12(9):2808-2830

485 Kiladis GN and Mo KC (1998) Interannual and intraseasonal variability in the Southern Hemisphere. In:
486 Karoly DJ and Vincent DG (ed) *Meteorology of the Southern Hemisphere*, Am Meteorol Soc, 410 pp

487 Kiladis, GN, Dias, J, Straub, KH, Wheeler, MC, Tulich, SN Kikuchi, K and Weickmann, KM, and
488 Ventrice, M. J. (2014) A comparison of OLR and circulation-based indices for tracking the MJO. *Mon.*
489 *Wea. Rev.*, 142, 1697-1715.

490 Kiladis, GN and KC Mo (1998) Interannual and Intraseasonal Variability in the Southern Hemisphere.
491 *Meteorology of the Southern Hemisphere*, Meteorol. Monorg., 49(27):307-336

492 Lau WKM and Waliser DE (2012) *Intraseasonal variability of the atmosphere-ocean climate system*, 2nd
493 edn. Springer, Heidelberg, Germany, pp. 613.

494 Liebmann B, Allured D (2005) Daily precipitation grids for South America. *Bull Am Meteorol Soc*
495 86(11):1567–1570

496 Liebmann B, Kiladis GN, Marengo JA, Ambrizzi T, Glick JD (1999) Submonthly convective variability
497 over South America and the South Atlantic convergence zone. *J Clim* 12:1877–1891

498 Liebmann B, Kiladis GN, Vera, CS, Saulo AC, Carvalho LMV (2004) Subseasonal variations of rainfall
499 in South America in the vicinity of the low-level jet east of the andes and comparison to those in the
500 South Atlantic convergence zone. *J of Clim* 17(19):3829-3842

501 Maharaj EA, Wheeler MC (2005) Forecasting an index of the Madden-oscillation. *Int. J. Clim* 25:1611–
502 1618

503 Martin, ER., Schumacher C (2011) Modulation of Caribbean precipitation by the Madden–Julian
504 oscillation. *J Clim* 24:813–824

505 Mo KC, Higgins RW (1998) The Pacific-South American modes and tropical convection during the
506 Southern Hemisphere winter. *Mon Weather Rev* 126(6):1581-1596

507 Muza MN, Carvalho LMV, Jones C, Liebmann B (2009) Intraseasonal and interannual variability of
508 extreme dry and wet events over southeastern South America and the subtropical Atlantic during austral
509 summer. *J Clim* 22(7):1682-1699

510 Naumann G, Vargas WM (2010) Joint diagnostic of the surface air temperature in southern South
511 America and the Madden-Julian oscillation. *Weather and Forecast* 25:1275-1280.
512 doi:10.1175/2010WAF2222418.1

513 Nogues-Paegle J, Mo KC (1997) Alternating wet and dry conditions over South America during summer.
514 *Mon Weather Rev* 125(2):279–291

515 Paegle JN, Byerle LA, Mo KC (2000) Intraseasonal modulation of South American summer
516 precipitation. *Mon Weather Rev* 128:837–850

517 Pai DS, Bhate J, Sreejith OP, Hatwar HR (2009) Impact of MJO on the intraseasonal variation of summer
518 monsoon rainfall over India. *Clim Dyn*. doi:10.1007/s00382-009-0634-4

519 Pohl B, Camberlin P (2006) Influence of the Madden-Julian oscillation on East African rainfall. I:
520 intraseasonal variability and regional dependency. *Q J of the R Meteorol Soc* 132(621):2521-2539

521 Revell MJ, Kidson, JW, Kiladis GN (2001) Interpreting low-frequency modes of Southern Hemisphere
522 atmospheric variability as the rotational response to divergent forcing. *Mon Weather Rev* 129(9):2416-
523 2425

524 Straub, K. H. (2013) MJO initiation in the Realtime Multivariate MJO Index. *J. Clim.*, 26, 1130-1151.

525 Vera C. et al. (2006) Toward a unified view of the American Monsoon Systems. *J Clim* 19:4977-5000

526 Wheeler MC, Hendon HH, Cleland S, Meinke H, Donald A (2009) Impacts of the Madden–Julian
527 oscillation on Australian rainfall and circulation. *J Clim* 22:1482–1498

528 Wheeler MC, Hendon HH (2004) An all-season real-time multivariate MJO index: development of an
529 index for monitoring and prediction. *Mon Weather Rev* 132:1917–1932

530 Zhang L, Wang B, Zeng Q (2009) Impact of the Madden-Julian oscillation on Summer Rainfall in
531 Southeast China. *J Clim* doi:10.1175/2008JCLI1959.1

532 Zhou S, L’Heureux M, Weaver S, Kumar A (2012) A composite study of the MJO influence on the
533 surface air temperature and precipitation over the Continental United States. *Clim Dyn* 38:1459–1471

534 Zhou Y, Thompson KR, Lu Y (2011) Mapping the relationship between Northern Hemisphere winter
535 surface air temperature and the Madden-Julian oscillation. *Mon Weather Rev* 139(8):2439-2454

536

537 **Figure Captions**

538 **Fig. 1** Composites of DJF 250 hPa geopotential height anomalies (shaded and contours) and 0.21 sigma-
539 level velocity potential (thick contours) according to RMM index-defined MJO phases 1 to 4 (expressed
540 on the bottom left of each panel) obtained with the regression model. The composites for MJO phases 5
541 to 8 are identical but with the sign reversed (expressed on the bottom right of each panel, see
542 Methodology). Only 95% significant values are shaded for the geopotential height anomalies. Contour
543 interval is 5 gpm and 0 contour is omitted. Velocity potential contour interval is $1 \times 10^7 \text{ m}^2 \text{ s}^{-1}$ and the first
544 contour is $2 \times 10^7 \text{ m}^2 \text{ s}^{-1}$; negative contours are dashed

545 **Fig. 2** As in Fig 1 but for MAM

546 **Fig. 3** As in Fig 1 but for JJA

547 **Fig. 4** As in Fig 1 but for SON

548 **Fig. 5** Coamplitude maps of 250 hPa geopotential height anomaly for each season

549 **Fig. 6** Cophase maps of negative 250 hPa geopotential height anomaly for each season. Each color

550 defines one of the 8 RMM phases of the MJO

551 **Fig. 7** Composites of DJF surface air temperature anomalies according to RMM index-defined MJO

552 phase 1 to 4 obtained with the regression model. The composites for MJO phases 5 to 8 are identical but

553 with the sign reversed, and those are indicated between parentheses (see Methodology). Only 95%

554 significant values are shown. Contour interval is 0.15 degrees Celsius and 0 contour is omitted

555 **Fig. 8** As in Fig 7 but for MAM

556 **Fig. 9** As in Fig 7 but for JJA

557 **Fig. 10** As in Fig 7 but for SON

558 **Fig. 11** DJF season (top and middle rows) composites of weekly rainfall probabilities for RMM index-

559 defined MJO phases 1 to 8. The probabilities refer to the chance of weekly averaged rainfall exceeding

560 the upper tercile, expressed as a ratio with the mean probability (nominally 33%) for every grid point.

561 Only 10% significant values are shown and those gridpoints with missing values were masked out in

562 grey. (bottom right) MJO composite of weekly rainfall probabilities for neutral MJO cases. (bottom left)

563 Climatological DJF mean weekly rainfall in South America. (bottom middle) Weekly rainfall threshold

564 **Fig. 12** As in Fig 11 but for MAM

565 **Fig. 13** As in Fig 11 but for JJA

566 **Fig. 14** As in Fig 11 but for SON

567 **Fig. 15** As in Fig 1 but using the OMI to generate the composite

568 **Fig. 16** As in Fig 4 but using the OMI to generate the composite

569 **Fig. 17** DJF season composites of weekly rainfall probabilities for OMI-defined MJO phases 1 to 8 and

570 neutral MJO cases. The probabilities refer to the chance of weekly averaged rainfall exceeding the upper

571 tercile, expressed as a ratio with the mean probability (nominally 33%) for every grid point. Only 10%

572 significant values are shown and those gridpoints with missing values were masked out in grey

573 **Fig. 18** As in Fig 17 but for SON

574

575

576

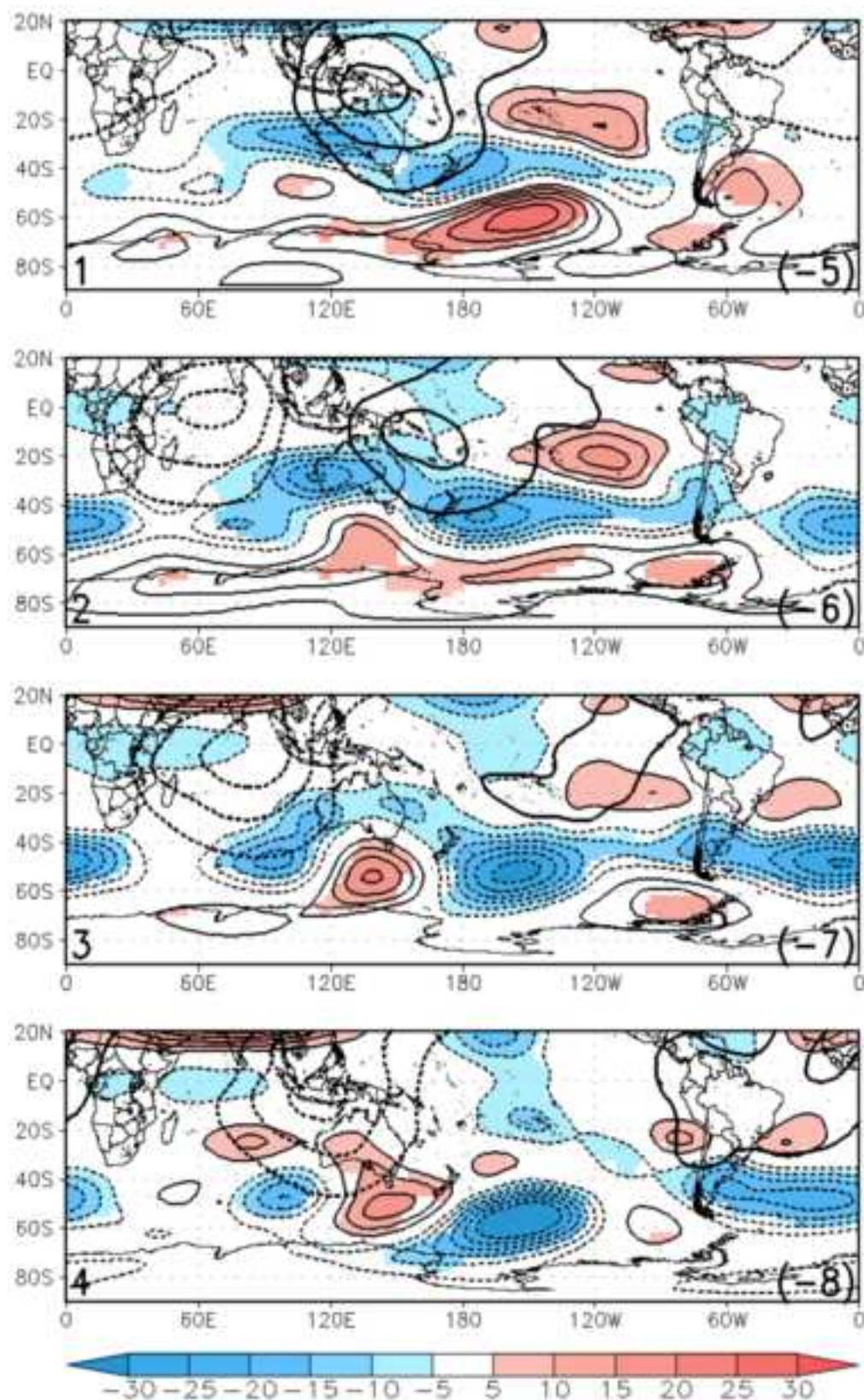


Fig. 1 Composites of DJF 250 hPa geopotential height anomalies (shaded and contours) and 0.21 sigma-level velocity potential (thick contours) according to RMM index-defined MJO phases 1 to 4 (expressed on the bottom left of each panel) obtained with the regression model. The composites for MJO phases 5 to 8 are identical but with the sign reversed (expressed on the bottom right of each panel, see Methodology). Only 95% significant values are shaded for the geopotential height anomalies. Contour interval is 5 gpm and 0 contour is omitted. Velocity potential contour interval is $1 \times 10^6 \text{ m}^2 \text{ s}^{-1}$ and the first contour is $2 \times 10^6 \text{ m}^2 \text{ s}^{-1}$; negative contours are dashed

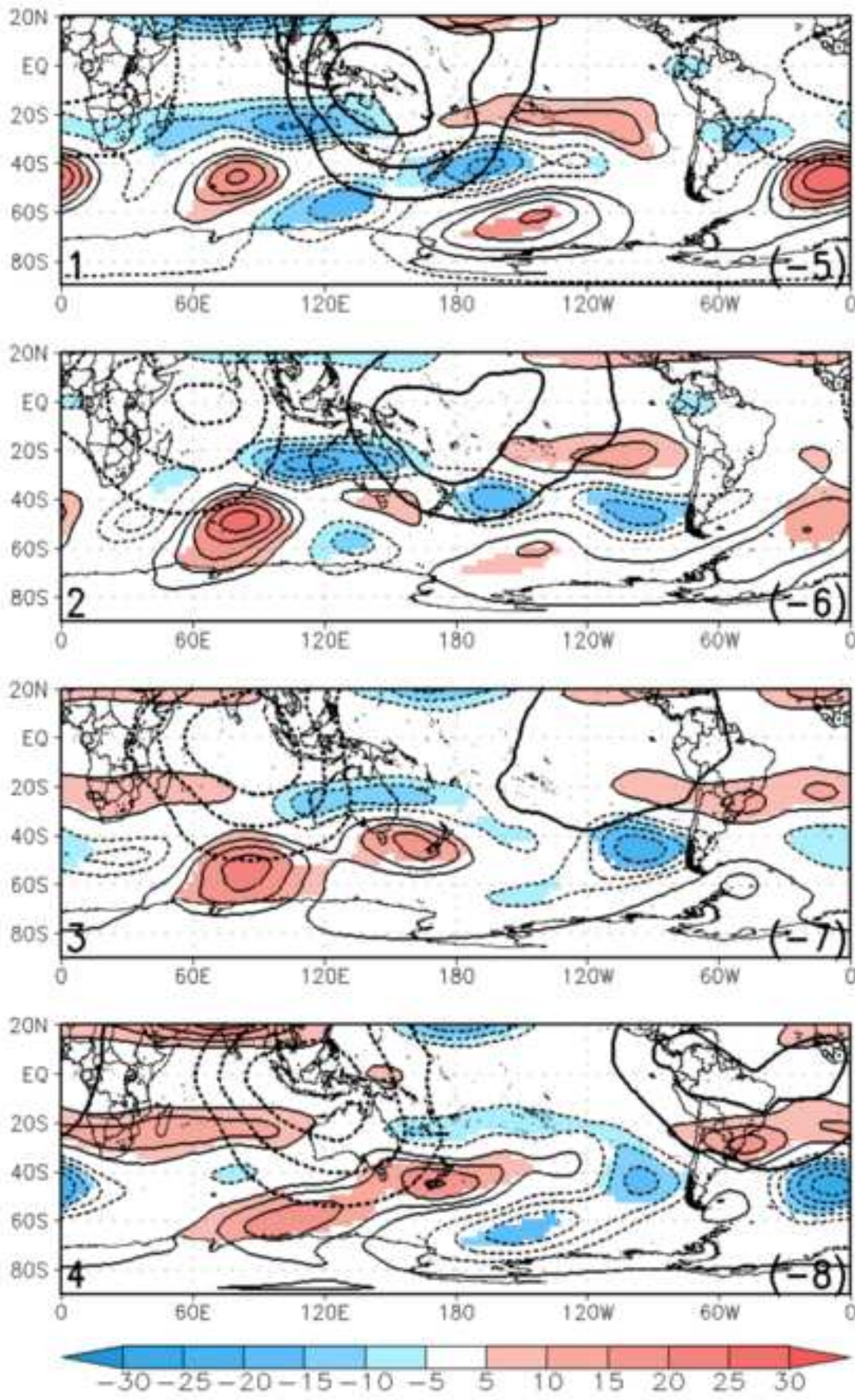


Fig. 2 As in Fig 1 but for MAM

Figure

[Click here to download high resolution image](#)

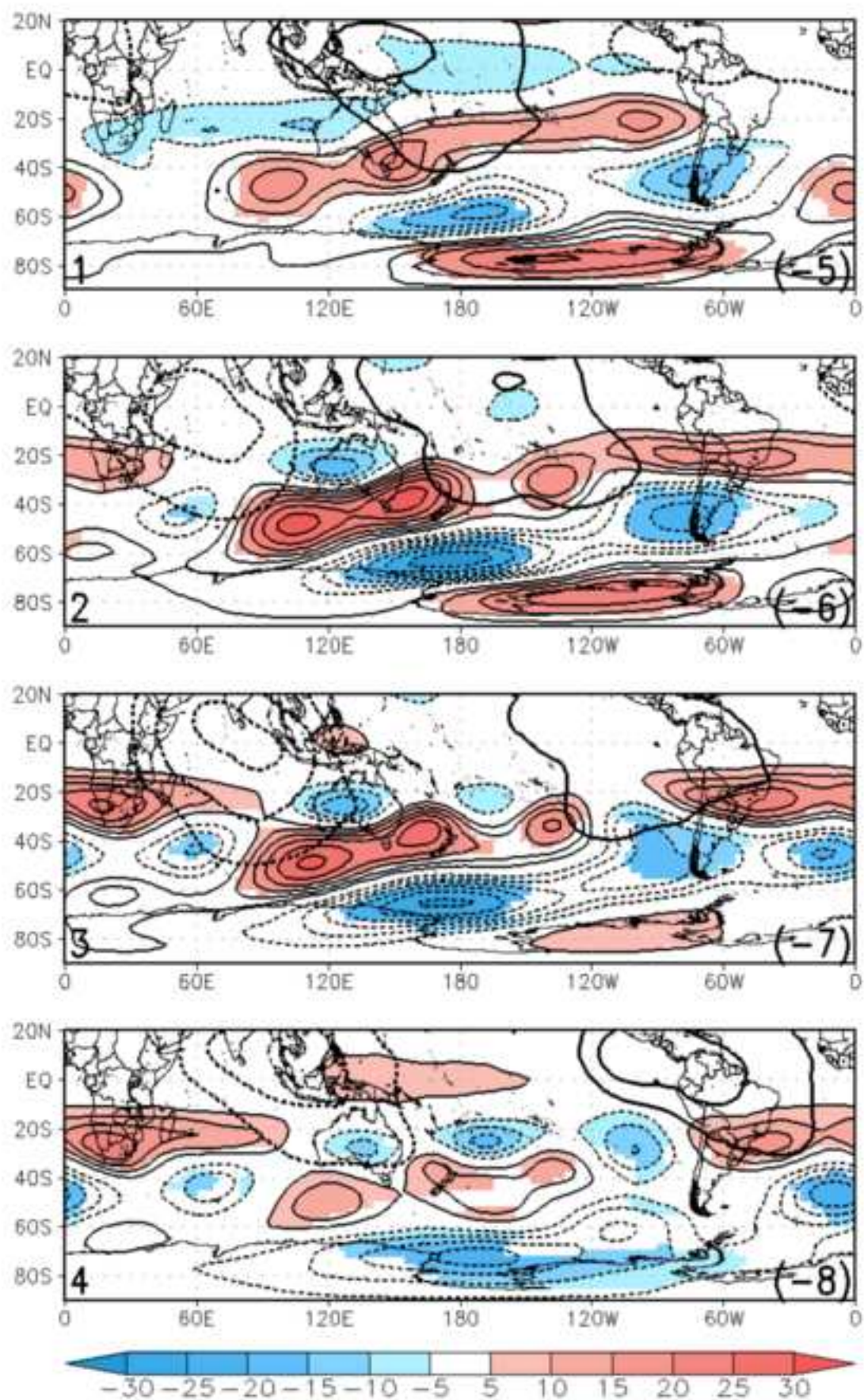


Fig. 3 As in Fig 1 but for JJA

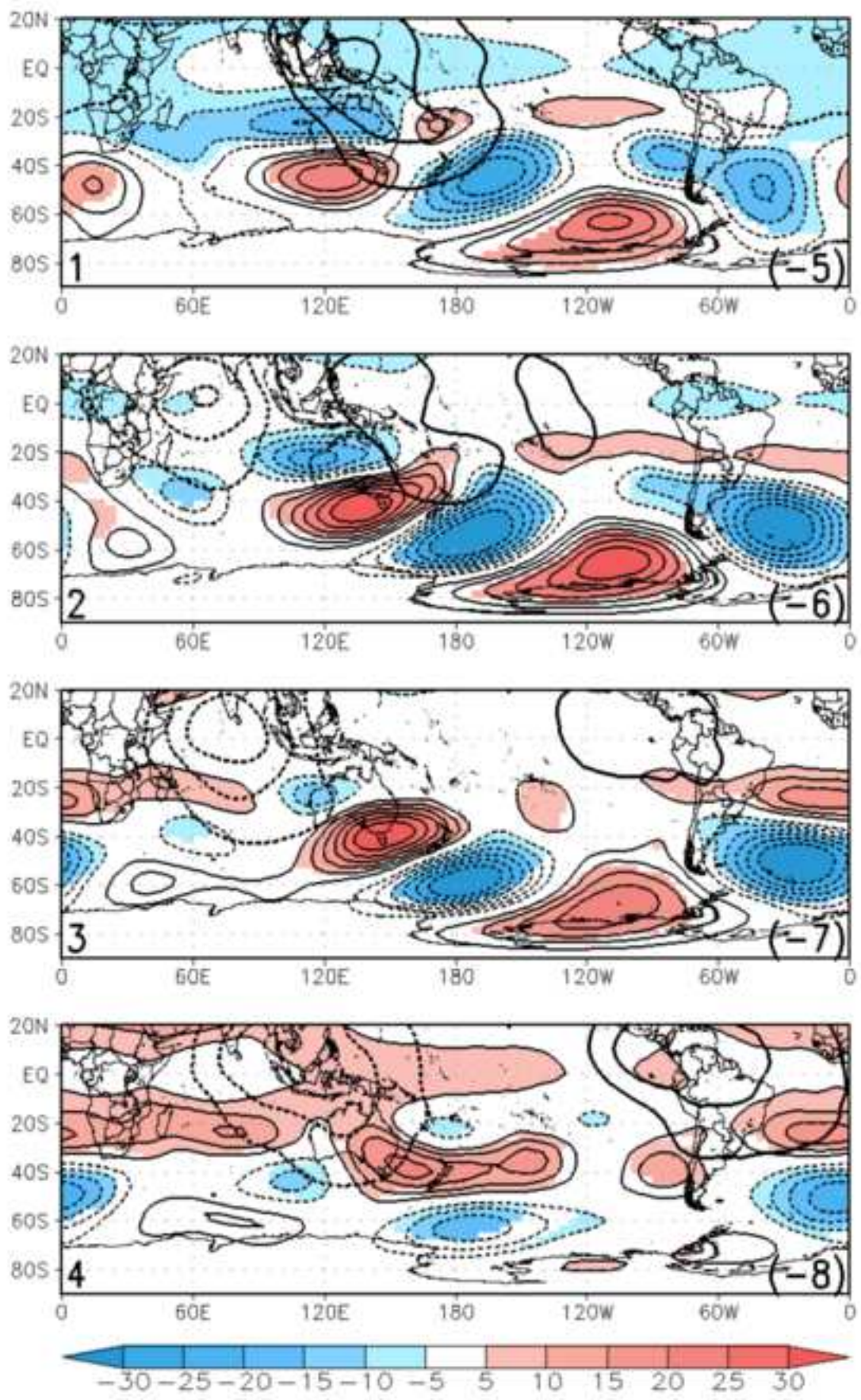


Fig. 4 As in Fig 1 but for SON

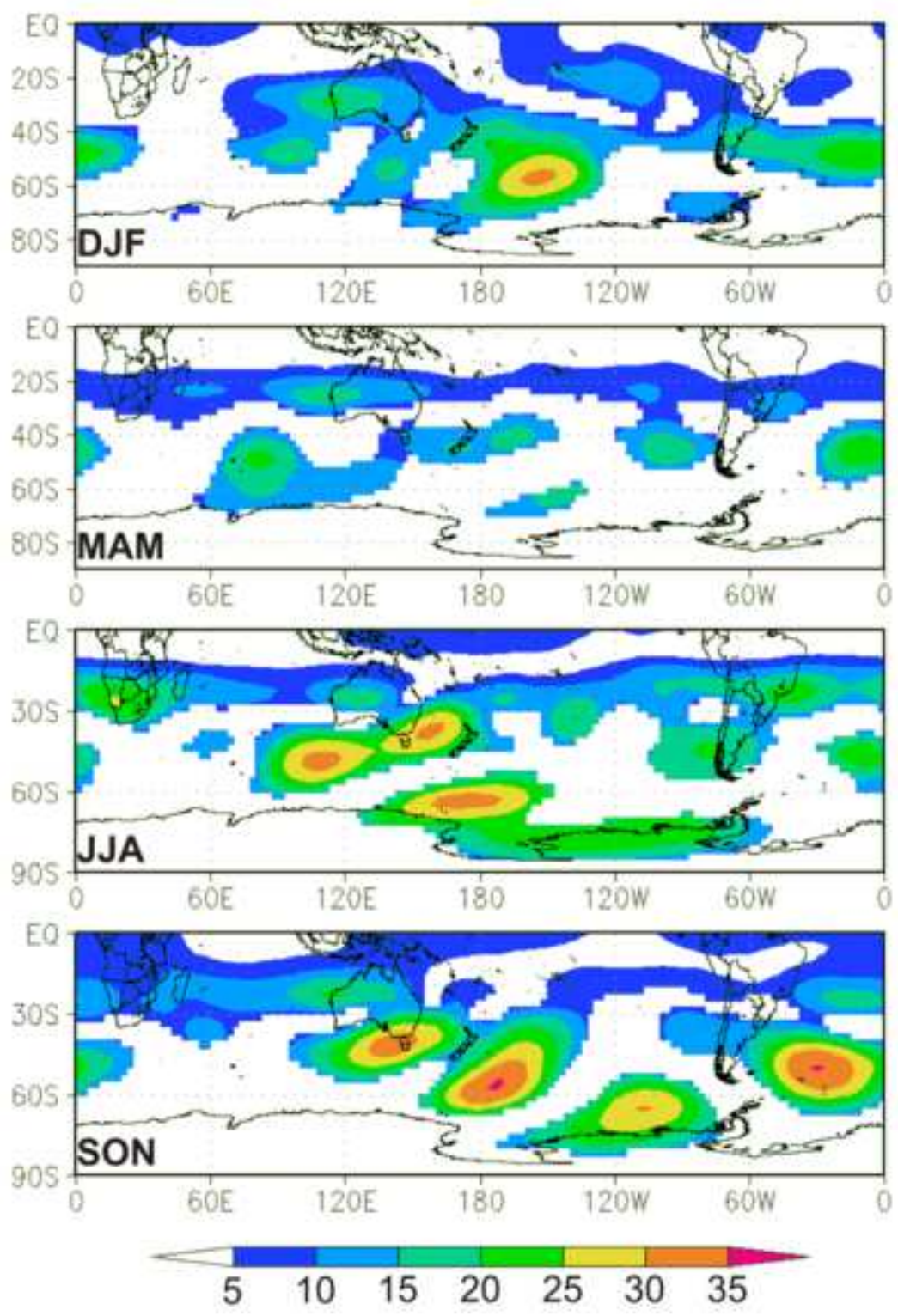


Fig. 5 Complitude maps of 250 hPa geopotential height anomaly for each season

Figure
[Click here to download high resolution image](#)

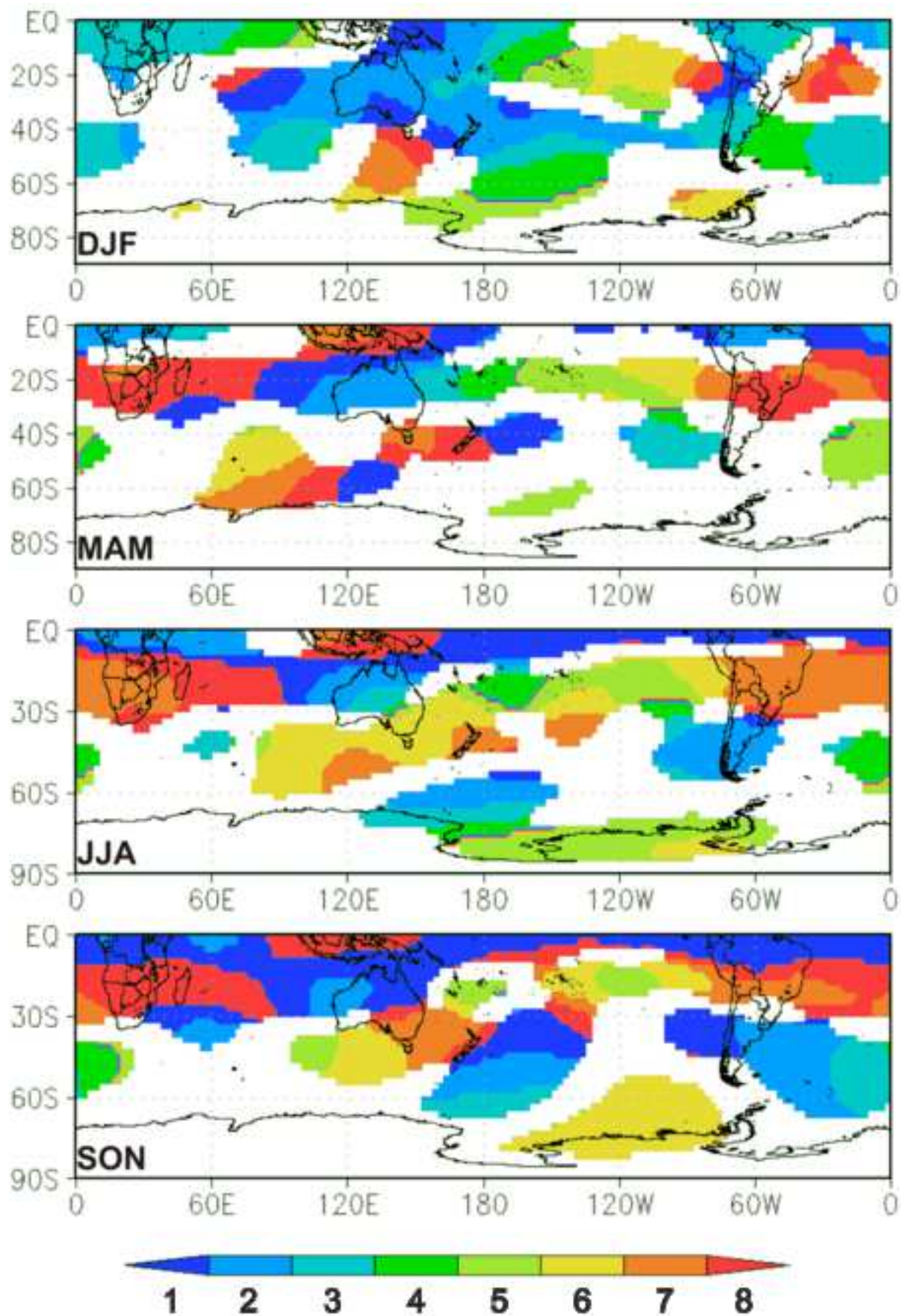


Fig. 6 Cophase maps of negative 250 hPa geopotential height anomaly for each season. Each color defines one of the 8 RMM phases of the MJO

Figure

[Click here to download high resolution image](#)

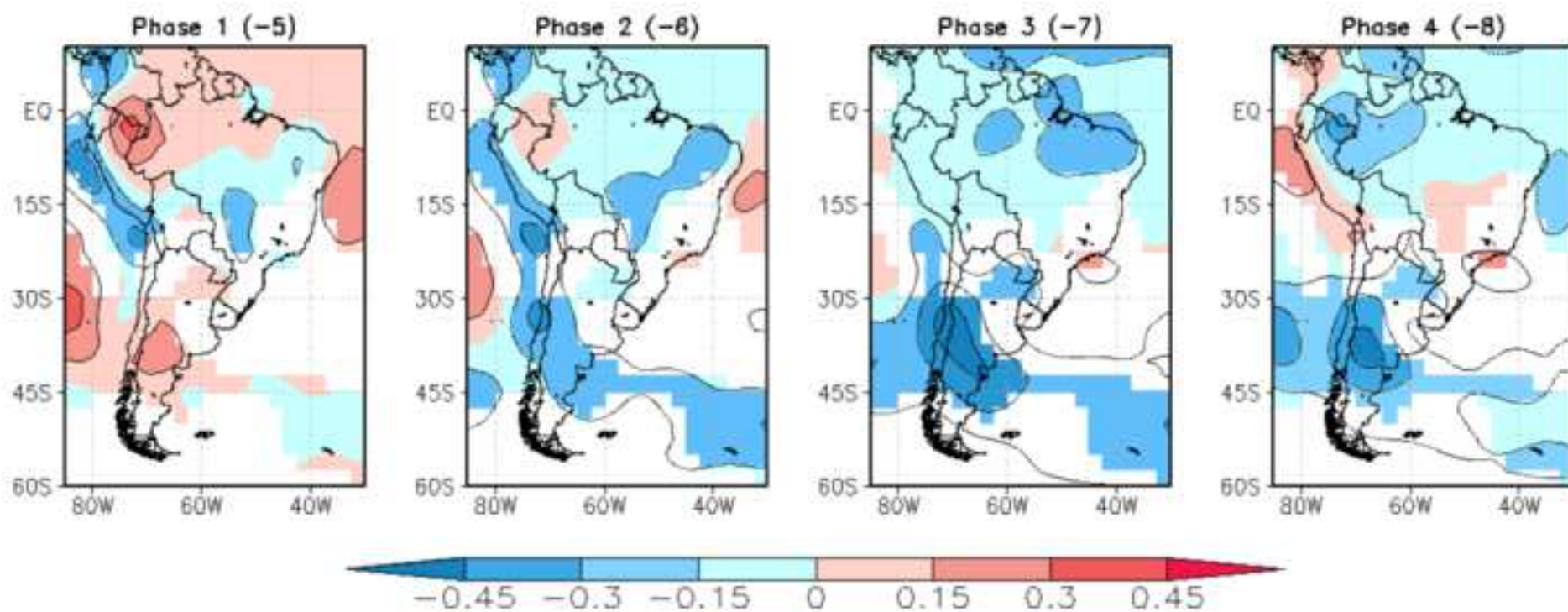


Fig. 7 Composites of DJF surface air temperature anomalies according to RMM index-defined MJO phase 1 to 4 obtained with the regression model. The composites for MJO phases 5 to 8 are identical but with the sign reversed, and those are indicated between parentheses (see Methodology). Only 95% significant values are shown. Contour interval is 0.15 degrees Celsius and 0 contour is omitted

Figure

[Click here to download high resolution image](#)

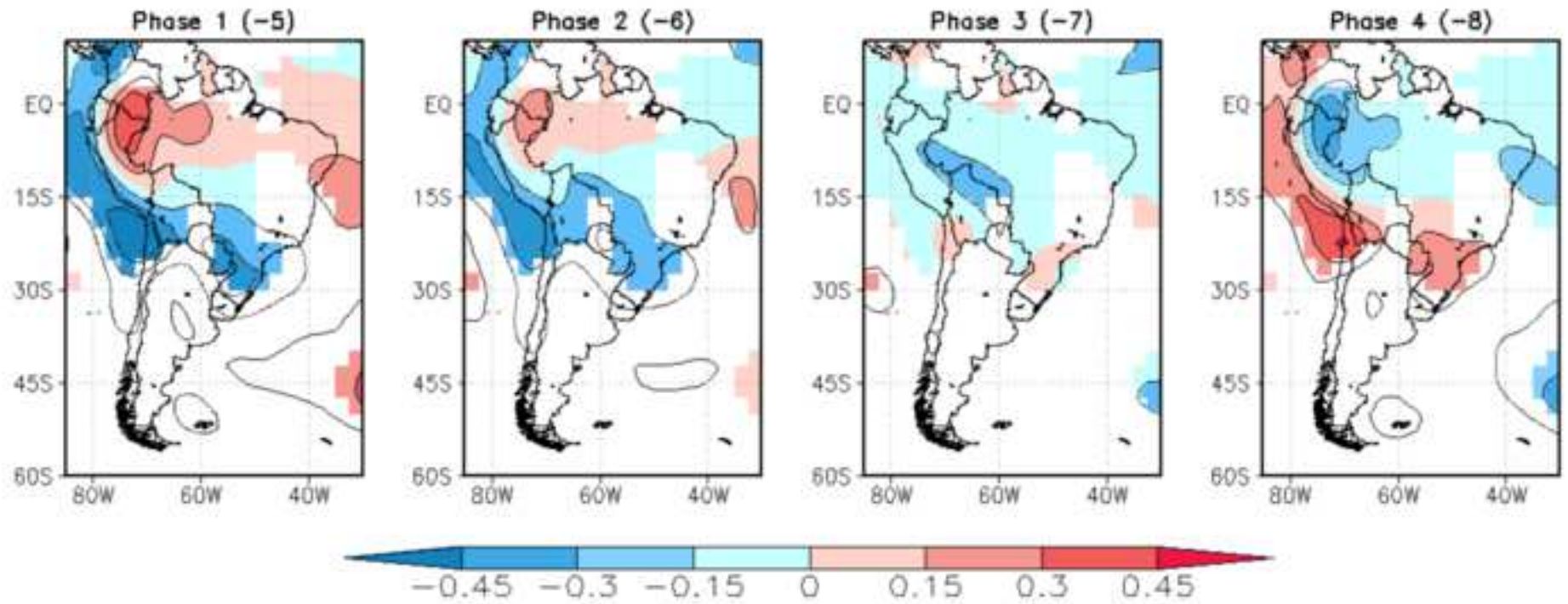


Fig. 8 As in Fig 7 but for MAM

Figure

[Click here to download high resolution image](#)

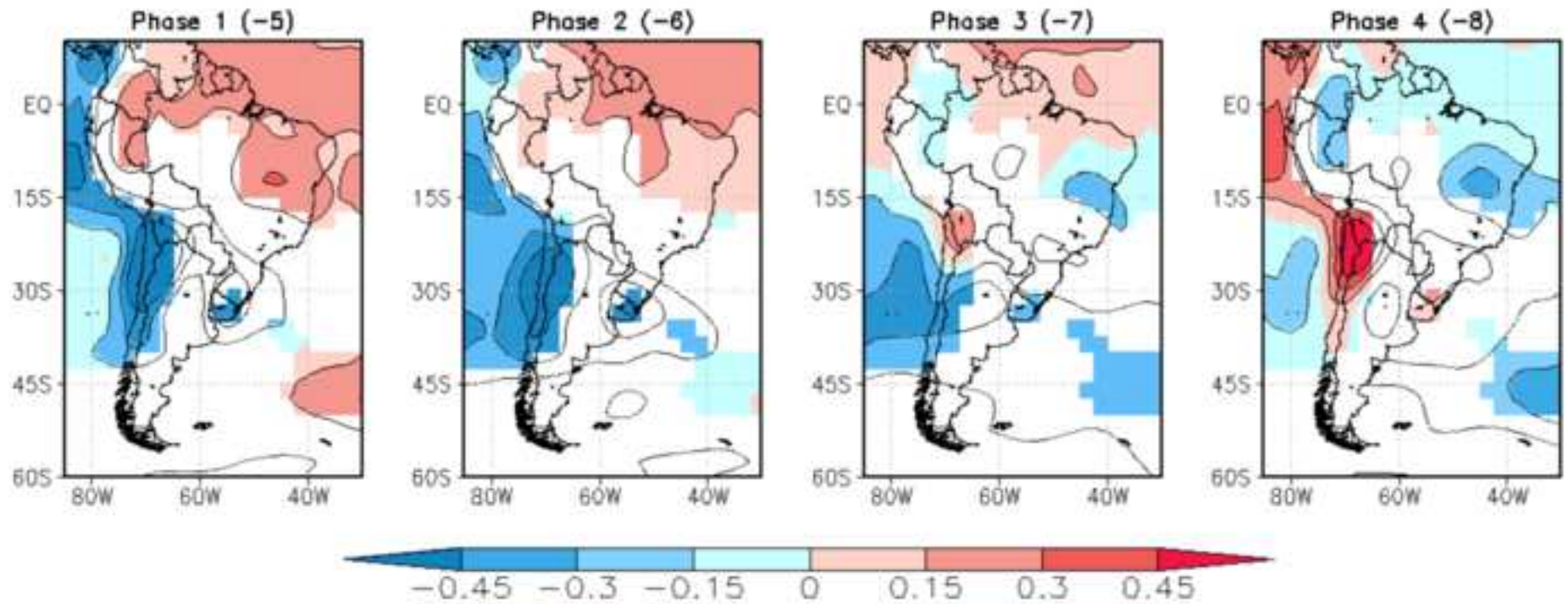


Fig. 9 As in Fig 7 but for JJA

Figure

[Click here to download high resolution image](#)

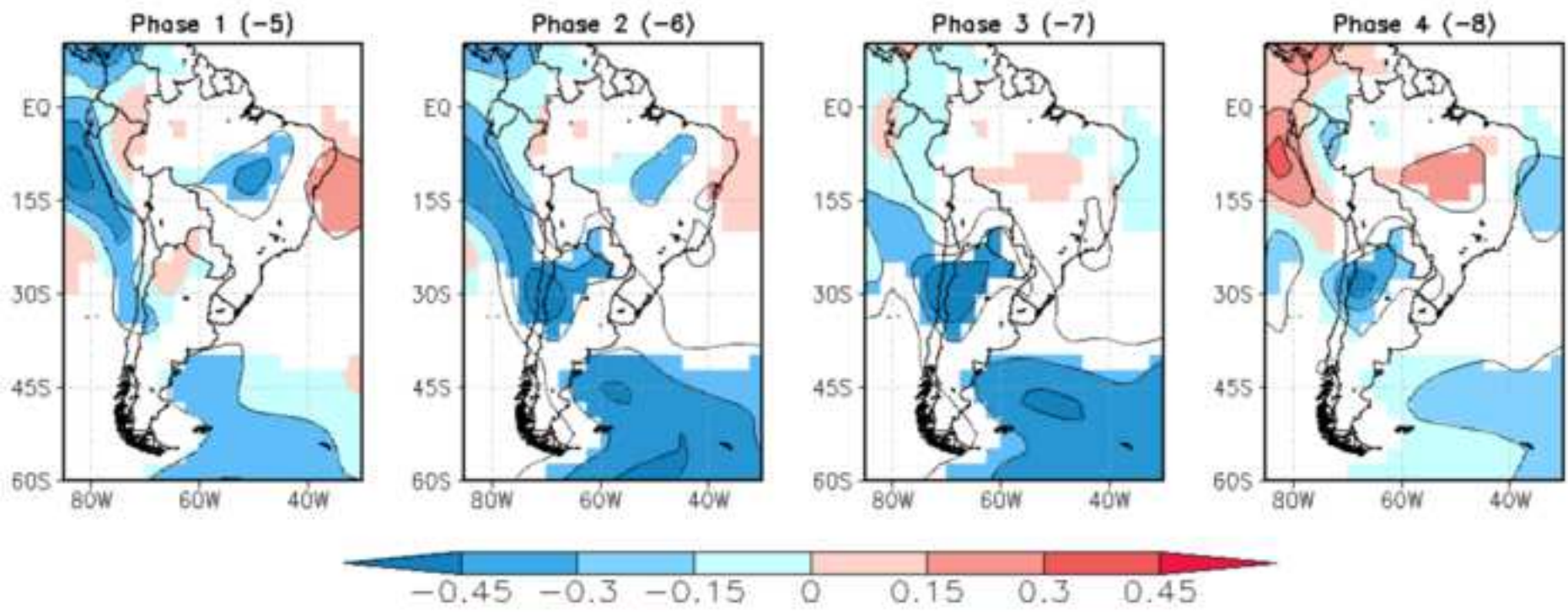


Fig. 10 As in Fig 7 but for SON

Figure

[Click here to download high resolution image](#)

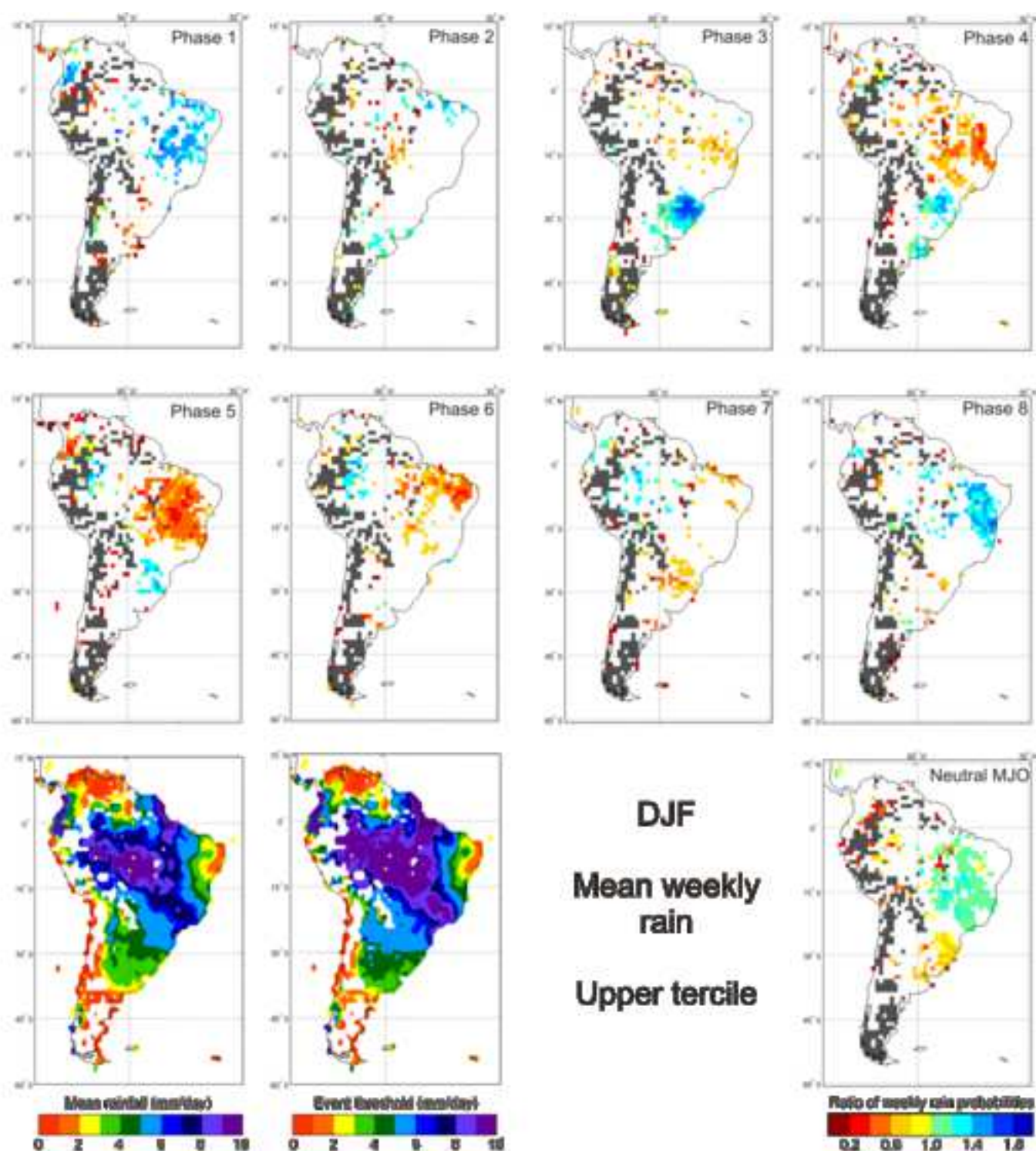


Fig. 11 DJF season (top and middle rows) composites of weekly rainfall probabilities for RMM index-defined MJO phases 1 to 8. The probabilities refer to the chance of weekly averaged rainfall exceeding the upper tercile, expressed as a ratio with the mean probability (nominally 33%) for every grid point. Only 10% significant values are shown and those gridpoints with missing values were masked out in gray. (bottom right) MJO composite of weekly rainfall probabilities for neutral MJO cases. (bottom left) Climatological DJF mean weekly rainfall in South America. (bottom middle) Weekly rainfall threshold

Figure
[Click here to download high resolution image](#)

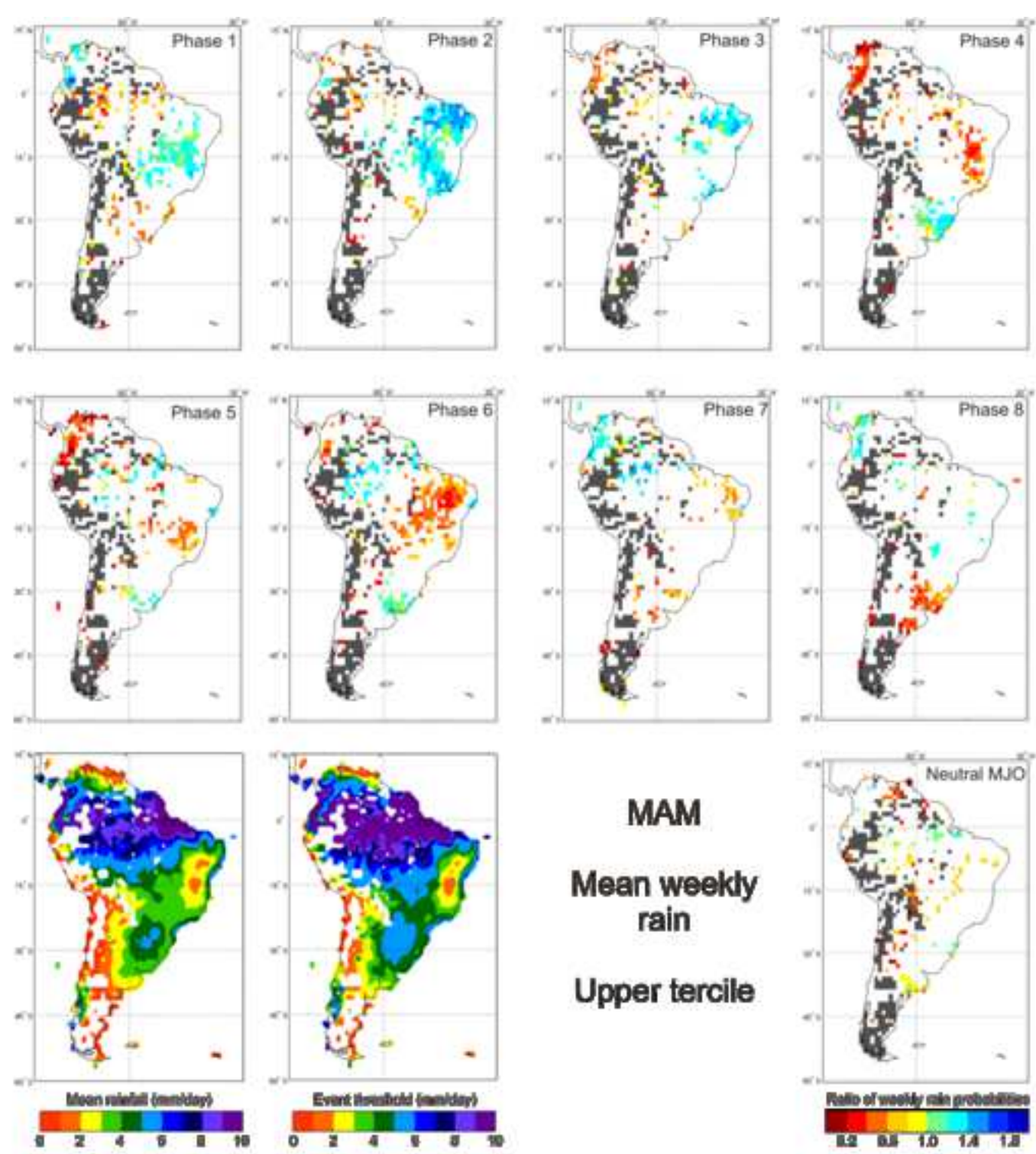


Fig. 12 As in Fig 11 but for MAM

Figure
[Click here to download high resolution image](#)

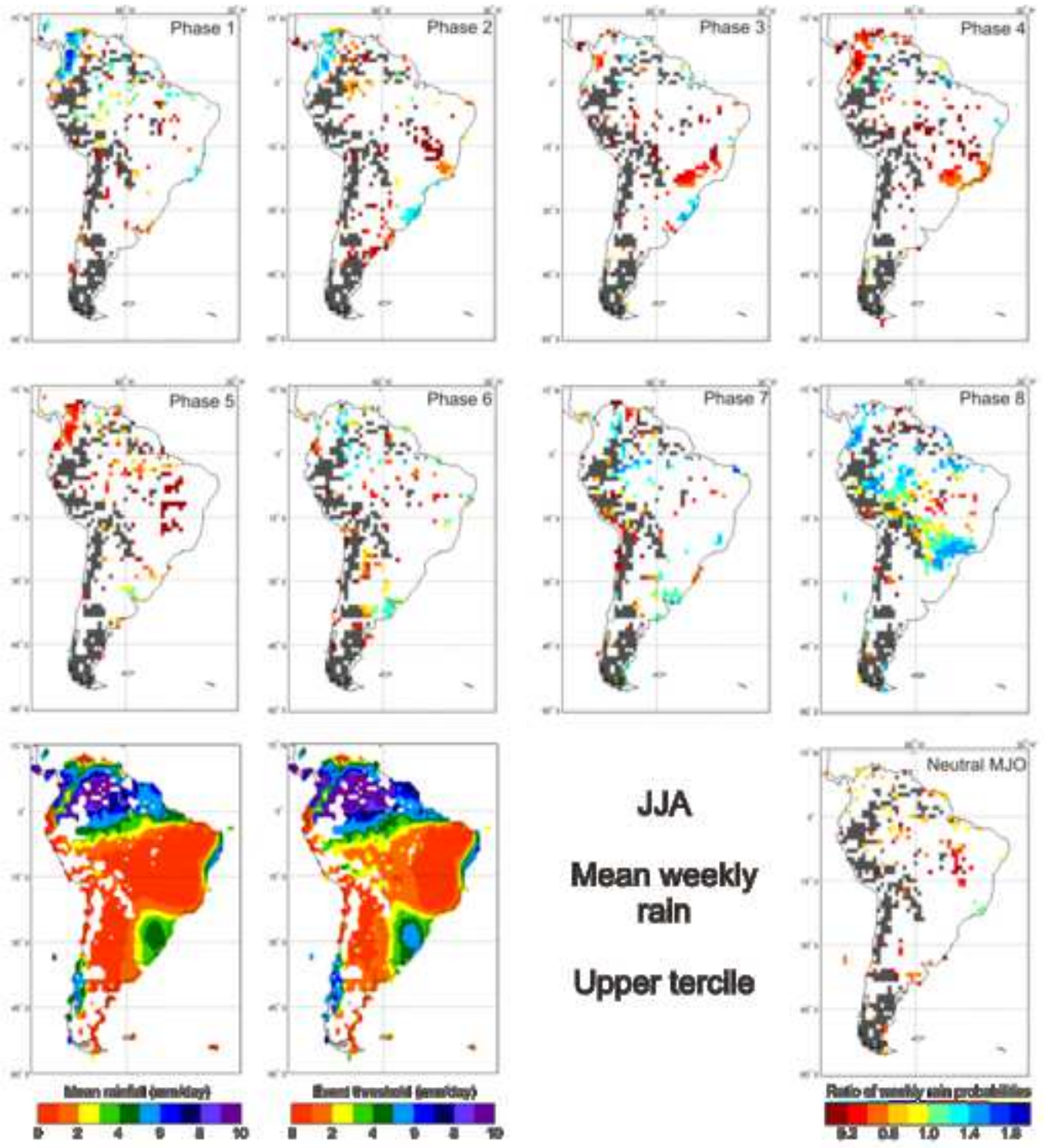


Fig. 13 As in Fig 11 but for JJA

Figure
[Click here to download high resolution image](#)

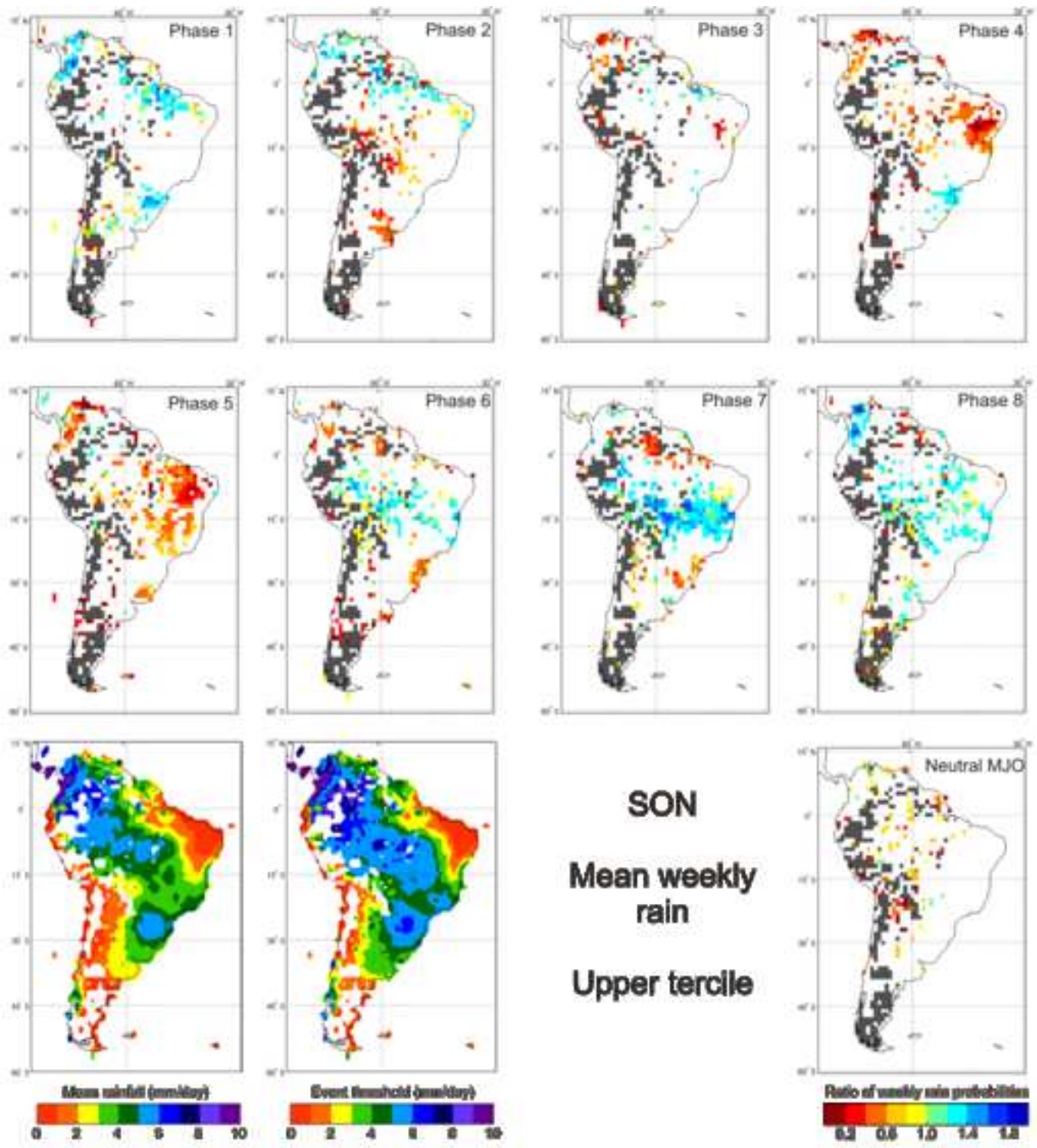


Fig. 14 As in Fig 11 but for SON

Figure
[Click here to download high resolution image](#)

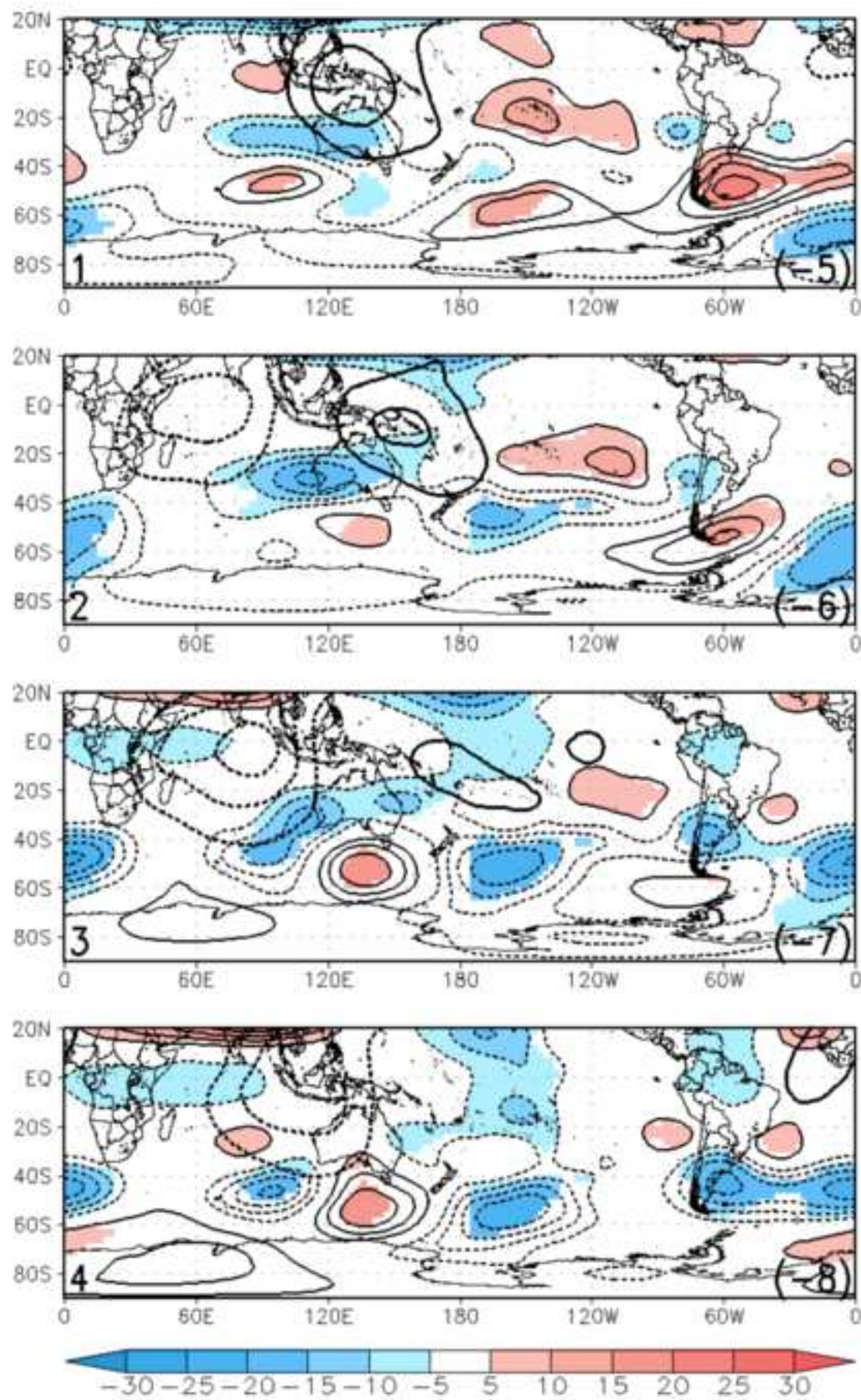


Fig. 15 As in Fig 1 but using the OMI to generate the composite

Figure
[Click here to download high resolution image](#)

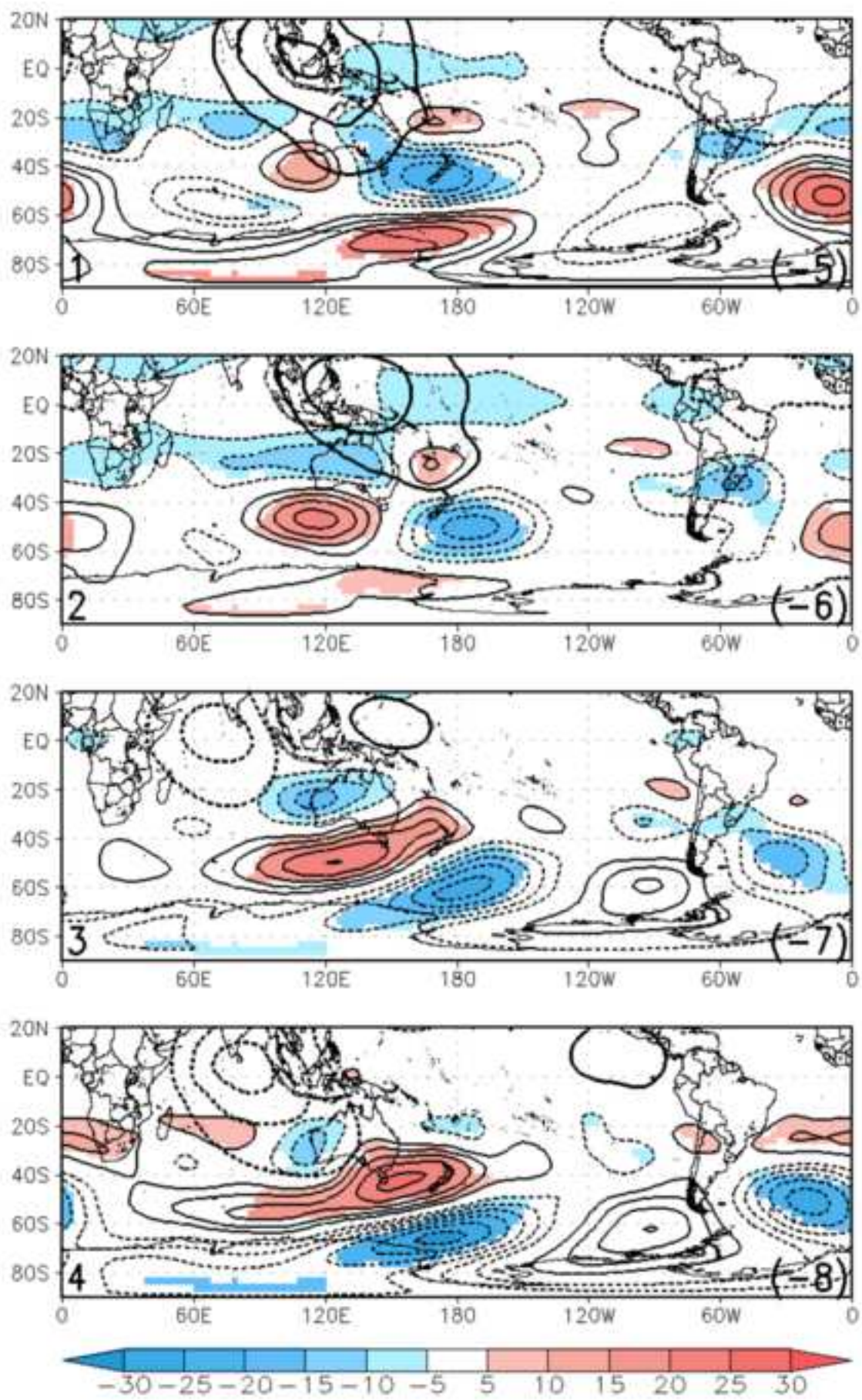


Fig. 16 As in Fig 4 but using the OMI to generate the composite

Figure

[Click here to download high resolution image](#)

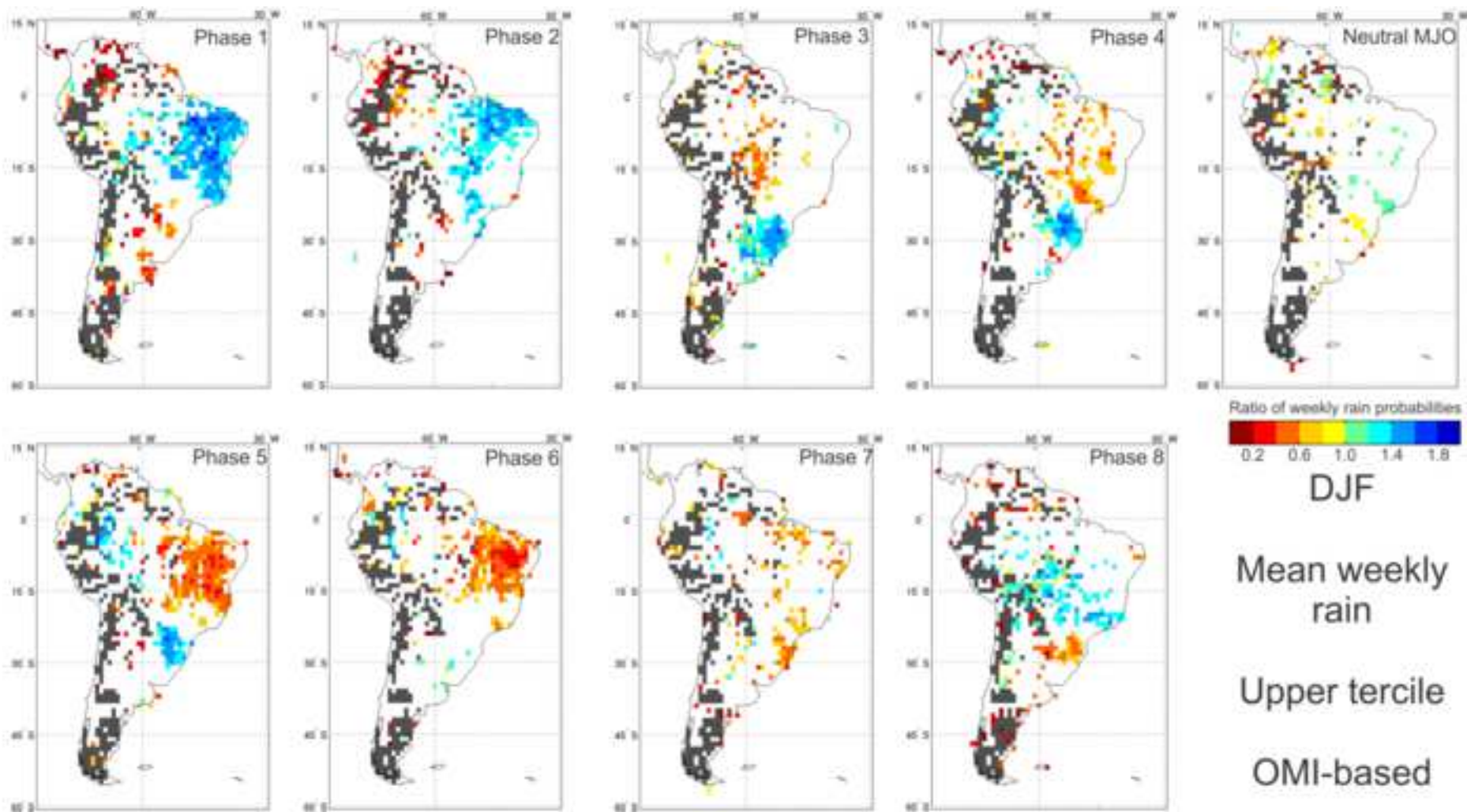


Fig. 17 DJF season composites of weekly rainfall probabilities for OMI-defined MJO phases 1 to 8 and neutral MJO cases. The probabilities refer to the chance of weekly averaged rainfall exceeding the upper tercile, expressed as a ratio with the mean probability (nominally 33%) for every grid point. Only 10% significant values are shown and those gridpoints with missing values were masked out in grey

Figure

[Click here to download high resolution image](#)

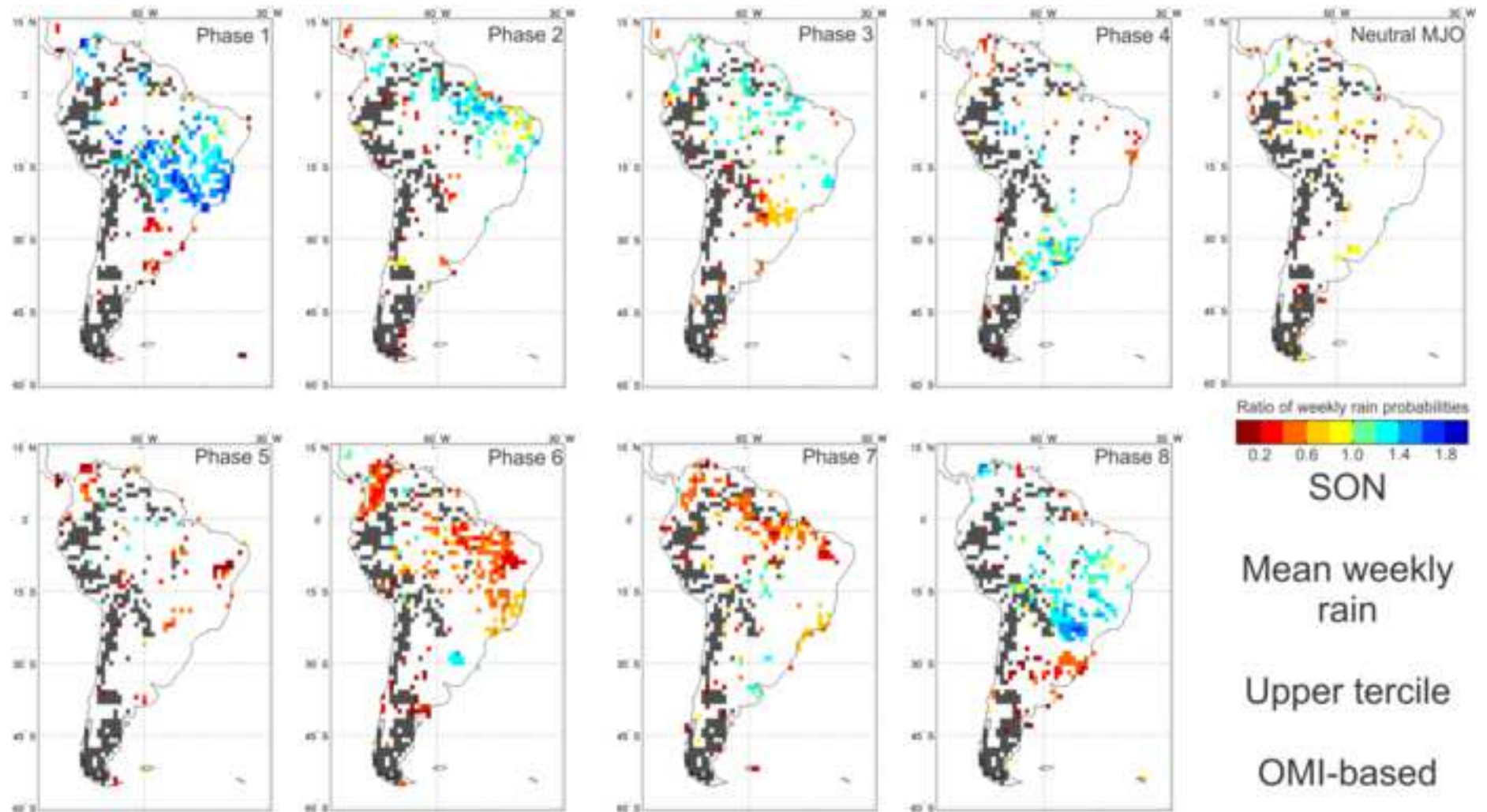


Fig. 18 As in Fig 17 but for SON